Geochemistry, Geophysics, Geosystems

RESEARCH ARTICLE

10.1029/2021GC010091

Key Points:

- Shear-wave splitting through A-, C-, and E-type olivine at upper mantle conditions shows azimuthal variations that differ
- A- and E-type reproduce polarity of observed fast orientation variation, with E-type predicting stronger delay times
- E-type olivine occurrence suggests a moderately hydrated asthenosphere in the Cascadia subduction zone back-arc

Supporting Information:

Supporting Information may be found in the online version of this article.

Correspondence to:

E. Löberich,
eric.loeberich@univie.ac.at

Citation:

Löberich, E., Long, M. D., Wagner, L. S., Qorbani, E., & Bokelmann, G. (2021). Constraints on olivine deformation from SKS shear-wave splitting beneath the southern Cascadia subduction zone back-arc. *Geochemistry, Geophysics, Geosystems*, *22*, e2021GC010091. https://doi.org/10.1029/2021GC010091

Received 11 AUG 2021
Accepted 29 OCT 2021

Author Contributions:

Conceptualization: E. Löberich, M. D. Long, L. S. Wagner, G. Bokelmann
Formal analysis: E. Löberich
Investigation: E. Löberich
Methodology: E. Löberich
Resources: M. D. Long, L. S. Wagner
Supervision: G. Bokelmann
Validation: M. D. Long, L. S. Wagner
Visualization: E. Löberich, E. Qorbani
Writing – original draft: E. Löberich
Writing – review & editing: M. D. Long, L. S. Wagner, E. Qorbani, G. Bokelmann

Constraints on Olivine Deformation From SKS Shear-Wave Splitting Beneath the Southern Cascadia Subduction Zone Back-Arc

E. Löberich[1], M. D. Long[2], L. S. Wagner[3], E. Qorbani[4], and G. Bokelmann[1]

[1]Department of Meteorology and Geophysics, University of Vienna, Vienna, Austria, [2]Earth and Planetary Sciences, Yale University, New Haven, CT, USA, [3]Earth and Planets Laboratory, Carnegie Institution for Science, Washington, DC, USA, [4]International Data Centre, CTBTO Preparatory Commission, Vienna, Austria

Abstract Shear-wave splitting observations of SKS and SKKS phases have been used widely to map azimuthal anisotropy, as caused by the occurrence of olivine, to constrain the dominant directions of upper mantle deformation. While SK(K)S splitting measurements at individual seismic stations are often averaged before interpretation, it is useful to consider additional information, for example, based on the variation of splitting parameters with azimuth due to the non-vertical incidence of core-phases. These constraints in theory enable a differentiation between various types of olivine and may allow us to infer otherwise poorly known upper mantle parameters such as stress, temperature, and water content. In this study, we predict the azimuthal variation of splitting parameters for A-, C-, and E-type olivine fabrics and match them with observations from the High Lava Plains, Northwestern Basin and Range, and Western Yellowstone Snake River Plain in the Pacific Northwest US. This helps to constrain the amount of water in the upper mantle in the back-arc of the Cascadia subduction zone, known for its consistent E-W oriented seismic anisotropy, and particularly large splitting delay times. Our investigation renders the C-type olivine mechanism improbable for this location; A- and E-type fabrics match the observations, although differentiating between them is difficult. However, the agreement of the amplitude of backazimuthal variation of the fast orientation, plus the potential to explain large splitting delay times, suggest the occurrence of E-type olivine, and thus the likely presence of a moderately hydrated upper mantle beneath Cascadia's back-arc.

Plain Language Summary Seismic anisotropy can elucidate upper mantle deformation. Lattice-preferred orientation of minerals such as olivine leads to shear-wave splitting that can be observed; it is related to the character of the deformation, e.g., the olivine fabric type. Since the occurrence of A-, C- and E-type relates to the amount of water, distinguishing these fabric types is particularly interesting. Yet, it has been difficult to differentiate between them so far due to similar shear-wave splitting they give rise to. Previous studies have not considered the slight dependence of the fast orientation with respect to the azimuth of the seismic arrival, which allows such a distinction in principle. Here, we study the E-W pattern of fast orientations in the southern Cascadia subduction zone back-arc, a region known for strong splitting. The comparison between observations and expectations shows that C-type cannot be present there. Since A- and E-type lead to similar fast orientations, distinguishing them is not trivial. Yet, the better fit between prediction and observation favors the presence of E-type fabric; an argument for the strong splitting and a moderately hydrated upper mantle beneath the study area.

1. Introduction

Seismic anisotropy offers the unique opportunity to constrain subsurface deformation and the mechanism behind it. For example, shear-waves that encounter anisotropy due to lattice-preferred orientation (LPO) of mineral assemblages experience polarization differences along their respective fast and slow propagation directions (Hess, 1964; Nicolas & Christensen, 1987; Savage, 1999; Silver & Chan, 1991). This type of anisotropy is most likely related to dislocation glide (Karato, 2008; Karato et al., 2008; Wenk, 1985). In terms of SKS and SKKS core-phases, the measured shear-wave splitting (SWS) parameters of fast orientation ϕ and delay time Δt (difference between fast and slow arrival times), are affected by upper mantle deformation along the raypath receiver side (e.g., Silver & Chan, 1991). The most common mineral in the upper mantle

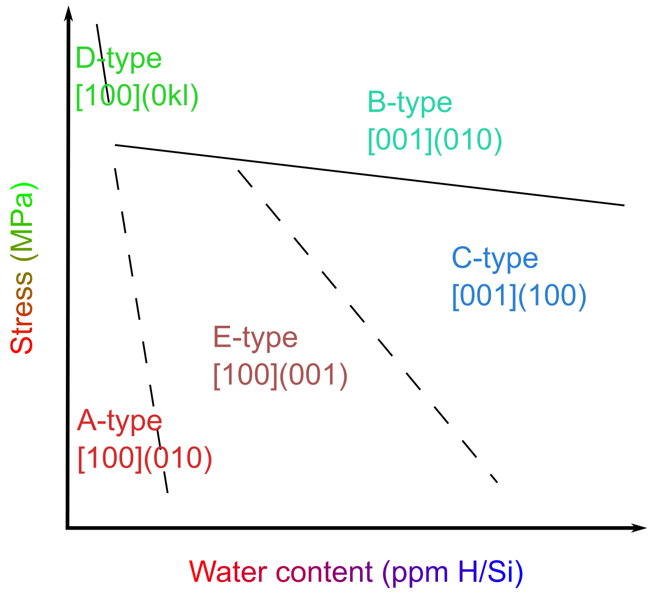

Figure 1. Scheme of the fabric diagram by Katayama et al. (2004) on the expected conditions (stress/water; $T = 1{,}470–1{,}570$ K) for olivine fabric types (see also Karato et al., 2008).

is olivine (e.g., McDonough & Rudnick, 1998), a mineral with orthorhombic symmetry (Babuska & Cara, 1991b; Mainprice, 2015) that plays a primary role in controlling seismic anisotropy (e.g., Bernard et al., 2021; Karato et al., 2008). The details of LPO formation are defined by upper mantle conditions (Karato et al., 2008), and depending on the olivine fabric type, the observed SWS pattern may be substantially different. As a consequence, SWS measurements may hold the potential to constrain olivine fabric types and therefore to infer the conditions of deformation (for example, temperature, stress, and water content).

Karato (1995) suggested that olivine LPO could be influenced by the presence of water, and subsequent work (Jung et al., 2006, and references therein) have elucidated the related causes. Following Jung et al. (2006), the individual manifestation of a given dominant slip system defines the LPO with respect to an applied deformation (based on van Houtte & Wagner, 1985). The dominant slip systems, in turn, are affected by the prevalent conditions under which the material is deformed. For olivine, a comparably minor percentage of water already affects the slip system manifestation (based on Mackwell et al., 1985). Jung et al. (2006) found that the presence of water in the olivine crystal structure facilitates [001] axis deformation. This study follows previous findings from Karato (1989) and Jung and Karato (2001a), who discovered increased grain boundary migration due to water, which might cause a changing LPO (based on Karato, 1987). In addition to water content, temperature conditions and deviatoric stress are crucial factors in determining the olivine slip system (Karato et al., 2008, and references therein).

Overall, according to their dominant slip system, five different olivine types (Figure 1) can be distinguished: [100](010) (A-type), [001](010) (B-type), [001](100) (C-type), [100](0 *kl*) (D-type) and [100](001) (E-type). B- and D-type olivine fabrics mainly occur at high stresses, while A-, C-, and E-type occur at lower stresses and are more likely to be prevalent in the asthenospheric upper mantle (e.g., Karato et al., 2008). Following the fabric diagram by Katayama et al. (2004), the transitions between A-, E-, and C-type fabrics are independent of stress, their respective presence thus constrains the possible amount of water. Jung et al. (2006) described these cases as follows. A-type occurs in dry environments at lower stress levels. This fabric is characterized by fast [100] axes that are aligned (sub)parallel to the shear direction (direction of maximum elongation), within the shear plane. Moreover, the slow symmetry axis [010] follows minimum elongation, perpendicular to the shear plane. In contrast, C-type occurs in a hydrated environment, resulting in the intermediate [001] axis aligning with the shear direction, while the fast axis [100] points in the direction of minimum elongation. E-type fabric develops in the presence of a moderate amount of water, between the conditions needed for A-type and C-type. Similar to the A-type, [100] aligns with the shear direction in E-type, but [001] is oriented perpendicular to the shear plane. Karato et al. (2008) related fabric variations to changing ambient conditions of deformation between lithosphere and asthenosphere. If the amount of water increases with depth (assuming high temperatures and low stress), A-type will be replaced by E- and subsequently C-type fabrics. In the case in which partial melting occurs, water will tend to partition into the melt, and the solid mantle will be drier and more likely to be dominated by A-type fabric (Karato, 1986; Karato et al., 2008). The deformation conditions in different geodynamic settings therefore play a crucial role in controlling the olivine fabric. Karato et al. (2008) (see also Jung & Karato, 2001b; Karato, 1995, 2004) argued that changing olivine fabrics influence observed anisotropy patterns across subduction zones. Similarly, they showed that a hydrated and hot plume environment may initiate an LPO transition, caused by partial melting between ∼100–150 km depth (Hirschmann, 2006; Karato et al., 2008). Consequently, asthenospheric areas that have been influenced by a rising plume may reveal a decreased amount of water and be dominated by A-type fabric.

The diversity of olivine fabric types in the upper mantle, and their relationships to deformation conditions suggested by laboratory experiments, imply that SWS observations may contain information about upper mantle parameters such as temperature, stress, and water content. However, it has proven difficult to distinguish among different olivine fabric types from actual SWS observations so far. Specifically, the known depth resolution problem (Savage, 1999; Silver & Chan, 1991), due to nearly vertical arrivals of core-phases such as SKS, is a challenge. Löberich and Bokelmann (2020a) recently showed that because the incidence angles of SKS waves are not perfectly vertical, the azimuthal variations of SWS parameters contain information about the details of olivine fabric and can be used to infer deformation geometry. In their study they used the large SWS data set of Liu et al. (2014) to determine an asthenospheric origin of observed SWS beneath Western and Central United States, constraining a mainly subhorizontally oriented flow plane of deformation, related to a high-temperature mechanism (Nicolas & Christensen, 1987). Since this approach enables distinguishing among plausible orientations of olivine fabric (in this example, A-type was assumed), differentiation between various olivine types might be possible as well if the deformation geometry is known or can reasonably be assumed.

Due to the assumptions required for our analysis (see further discussion in Section 3), we must select an area of interest that shows indications of a dominant single-layer case of seismic anisotropy that likely corresponds to horizontal simple shear in the asthenosphere (unlike Löberich & Bokelmann, 2020a, who considered lithospheric and asthenospheric deformation geometries). We assume that the related simple SWS pattern is due only to olivine fabric. To a lesser degree, upper mantle anisotropy could be also affected by orthopyroxene, clinopyroxene, and garnet (Babuska & Cara, 1991a; Karato, 2008; Mainprice, 2015; Nicolas & Christensen, 1987), but olivine is generally considered to dominate upper mantle anisotropy (e.g., Bernard et al., 2021). While in Löberich and Bokelmann (2020a) a large study area was investigated assuming a constant olivine fabric, a test site of regional scale seems more appropriate when considering laterally varying olivine types. As demonstrated in Löberich and Bokelmann (2020b) for the Central European Alps, our approach might be also applicable on this scale. However, the reduced number of observations and poorer backazimuthal coverage could make it more difficult to elucidate the actual variation in a small area, unless a region with favorable data coverage is carefully chosen.

In this study, we will investigate the backazimuthal distribution of SWS measurements to determine the dominant olivine fabric beneath the High Lava Plains (HLP), Northwestern Basin and Range (B&R) and Western Yellowstone Snake River Plain (YSRP) (according to e.g., Ford et al., 2013, and references therein). Based on the comparison of actual and expected variations, we aim to distinguish between A-, C-, and E-type olivine to infer the likely water content in the upper mantle in this back-arc section. Together with information on the large-scale flow geometry (e.g., Druken et al., 2011; Zhou et al., 2018) and comparisons with distributions of low-velocity anomalies (Wagner et al., 2013), melts (Debayle et al., 2020), and azimuthal surface wave anisotropy (Wagner et al., 2013), we discuss our constraints on olivine fabric types in the geodynamic framework of the Cascadia subduction zone (CSZ) back-arc setting.

2. Pacific Northwest US

2.1. Choosing the Study Area

During the initial investigation of the Liu et al. (2014) data set, documented in Löberich and Bokelmann (2020a), the area spanned by HLP, Northwestern B&R, and Western YSRP raised our interest due to the high station density, the continuous pattern of ϕ, and the occurrence of unusually high Δt values (Liu et al., 2014; Long, 2016; Long et al., 2012; Wagner & Long, 2013, and references therein). Since the lithosphere is very thin in this region of the CSZ back-arc, we do not expect distinct lithosphere and asthenosphere layers of anisotropy. Indeed, previous detailed SWS studies of the HLP region (Long et al., 2009; Wagner & Long, 2013) showed that there is little or no variability in apparent splitting parameters with backazimuth, arguing for a single layer. This assumption is supported by the observed low standard deviations σ_ϕ, associated with a simple scenario of upper mantle anisotropy, unveiled by the Complex Anisotropy Index (Liu et al., 2014). Hence, multiple anisotropic layers, which could lead to a 90° periodicity with azimuth in SWS parameters (e.g., Qorbani et al., 2015), or a dipping symmetry axis, which would introduce a 360° periodicity, are unlikely to be present in the CSZ back-arc. It must be mentioned that Yuan and Romanowicz (2010) argued for multiple layers of anisotropy beneath the Pacific Northwest (PNW) based on the joint inversion of surface waves and SKS splitting. However, most other models do not include multiple layers; for example, a significant change in anisotropy orientation with depth was not identified in a recent study of

Mondal and Long (2020) in the HLP. In their model, based on SKS splitting intensity tomography, ϕ shows only very weak variability with depth down to 400 km. In order to define the bounds of our study area in the CSZ back-arc, we relied on the surface wave phase velocity measurements of Wagner and Long (2013), who identified a particularly consistent orientation of anisotropy in upper mantle depths at a period of 66 s. The spatial distribution of this mainly E-W oriented pattern of azimuthal anisotropy defines the extension of our study area.

2.2. Tectonic Setting and Seismic Structures

Figure 2 shows the plate tectonic setting in the Pacific Northwest and outlines the study area in the back-arc of the CSZ. This convergent plate boundary is formed by the oceanic Explorer, Juan de Fuca, and Gorda plates on one side, and the continental North American plate on the other. While the denser oceanic lithosphere moves northeastwards and is subducted, the lighter continental lithosphere overrides it, moving southwestwards (Eakin et al., 2010; Gripp & Gordon, 2002). Numerous studies have considered its slab geometry up to ∼400–500 km depth, consistently showing a slab dipping ∼50–60° eastwards (Eakin et al., 2010; Hayes et al., 2018; Obrebski et al., 2010; Xue & Allen, 2007).

The subduction zone has evolved through time to its current tectonic setting, with Farallon slab (FS) subducting beneath North America beginning 150 Ma ago (Long, 2016; Severinghaus & Atwater, 1990). In the course of this process, the Siletzia terrane was accumulated to the continental lithosphere (55 Ma), initiating the Gorda-Juan de Fuca subduction further west (Grunder et al., 2017). The Gorda-Juan de Fuca slab (G-JdFS) likely steepened and started rolling back ∼18 Ma ago (Long et al., 2012; Schellart et al., 2010), associated with migration of the trench. Long et al. (2012) indicates that this transition led to significant upwelling in the back-arc mantle; according to Grunder et al. (2017), it was accompanied by the clockwise rotating fore-arc and faulting processes in the B&R. Further, Long et al. (2012) suggested that this upwelling may have produced the mantle melting and volcanism of the Columbia River flood basalts, while other models invoke the Yellowstone plume impinging on the lithosphere as the cause of the flood basalt eruptions (Darold & Humphreys, 2013; Grunder et al., 2017; Obrebski et al., 2010; R. B. Smith et al., 2009; Xue & Allen, 2007). Druken et al. (2011) and Long et al. (2012) suggested that ongoing slab rollback controls the present-day E-W flow field (see also Zandt & Humphreys, 2008), including a toroidal flow contribution and sustained upwelling. Over the past 10.5 Ma, this flow geometry may have led to the accumulation of melts in the uppermost mantle due to decompression melting. The orientation of the time-progressive volcanic track in the HLP toward the west may map the transient position of melt accumulation (Grunder et al., 2017; Long et al., 2012). Long (2016) later discussed the possibility that the G-JdFS is fragmented at depth, allowing for horizontal mantle flow through a slab window, rather than the toroidal flow field induced by slab rollback. Further, Long (2016) argued that regardless of the possible presence of the Yellowstone plume in the upper mantle, the present-day flow field beneath our study area is simple, is dominated by E-W flow, and is controlled by the motions of the slab in rollback subduction, with or without a slab gap.

The remnants of the PNW's complex tectonic history are visible in the modern upper mantle structures imaged in tomographic models (e.g., Obrebski et al., 2010; Gao & Shen, 2014; Wagner & Long, 2013; Wagner et al., 2010). To get an overview on the geometry and distribution of potentially influencing structures below the study area, we extract shear-wave velocity perturbations ($dV/V \leq -3\%$ or $dV/V \geq 2\%$) of the HLP2010 model by Wagner et al. (2010). The corresponding positive and negative anomalies extend between ∼3.2–214.5 km and ∼2.5–144.5 km depth, respectively. Figure 2 shows their lateral extent at the bottom of each structure, based on the contours of maximum depth reached in the upper mantle. Large-scale velocity anomalies of different polarity beneath the PNW become apparent. In agreement with the model of Long et al. (2012), and the likelihood of accumulated decompressional melts (see also Gao & Shen, 2014), the study area is affected by a low-velocity body of broad lateral extent. Following the Yellowstone and HLP volcanic tracks, this structure further expands along the YSRP toward the Yellowstone Caldera in the northeast and reaches the Cascade Arc (CA) and Newberry Caldera in the west. The anomaly itself generally concentrates in depths of ∼90 km, but also indicates variation across the upper mantle. This low-velocity structure tends to broaden at shallower depths above the G-JdFS and extends deeper in the Northwestern B&R, the HLP-YSRP border region, and north of the Yellowstone Caldera. The appearance of high-velocity bodies, namely the Idaho curtain (IC) (according to Stanciu & Humphreys, 2020), the G-JdFS and the Wyoming

10.1029/2021GC010091

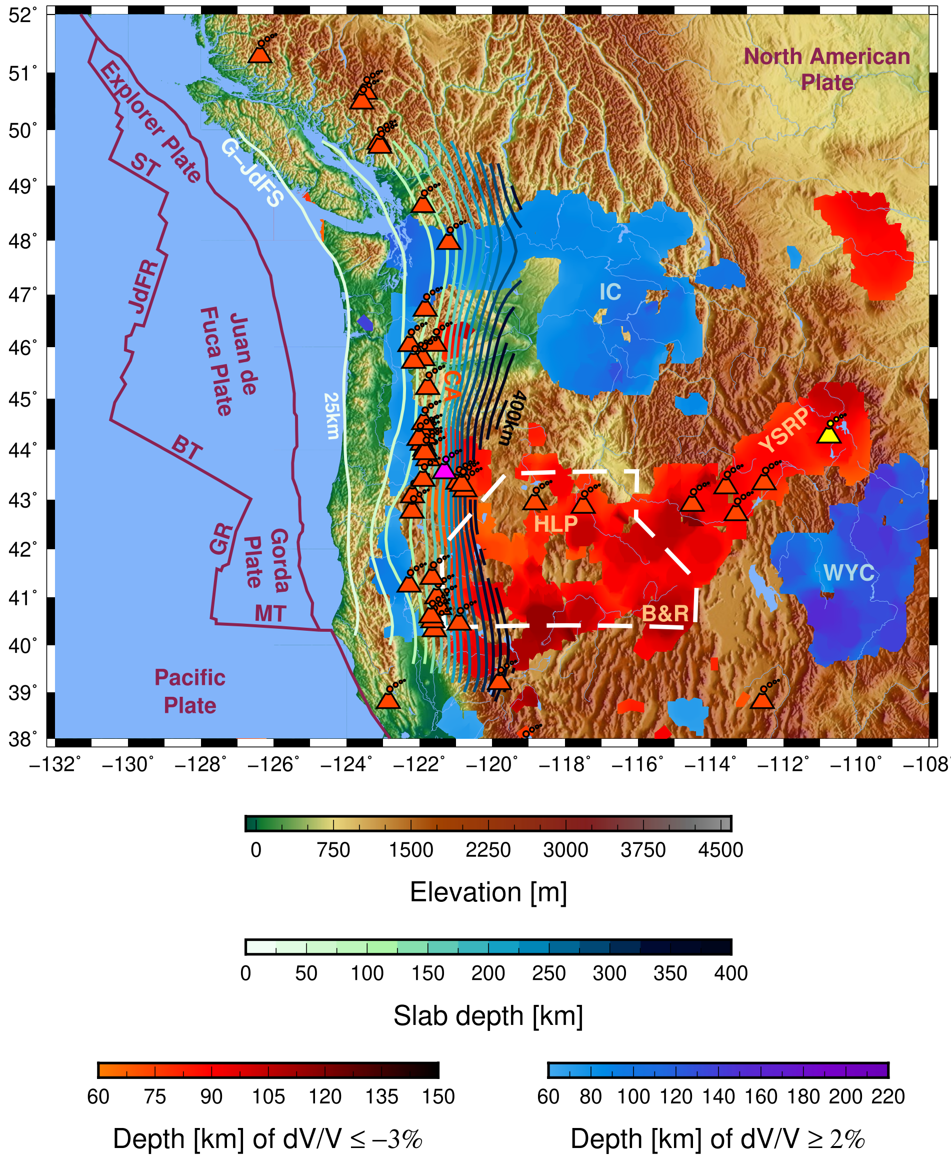

Figure 2. Tectonic setting (based on Long, 2016; Xue & Allen, 2007) for the study area (dashed, white polygon) in the Pacific Northwest, and depth distribution of tomographic anomalies. Position of plate boundaries (solid, burgundy lines; BT, Blanco Transform; MT, Mendocino Transform; ST, Sovanco Transform; GR, Gorda Ridge; JdFR, Juan de Fuca Ridge) are taken from Bird (2003); the Gorda-Juan de Fuca slab (G-JdFS) depth distribution (colored contours) is determined based on Hayes et al. (2018) between 25 and 400 km. Shear-wave velocity perturbations dV/V are adapted from the HLP2010 model of Wagner et al. (2010). They show depth contours in the upper mantle in which the threshold (low-velocity: −3%, high-velocity: 2%) is still reached or surpassed (IC, Idaho curtain; WYC, Wyoming craton; B&R, Basin and Range; HLP, High Lava Plains; YSRP, Yellowstone Snake River Plain). The locations of volcanoes (orange symbols) on land (e.g. along CA: Cascade Arc) are taken from the Smithsonian Institution GVP (2002); Yellowstone Caldera (yellow volcano) and Newberry Caldera (magenta volcano) are highlighted.

craton (WYC), limit further extension of the low-velocity body to the north, west and southeast. As indicated before, whether the G-JdFS is continuous in the upper mantle (e.g., Wagner et al., 2010), or contains a slab gap (e.g., Obrebski et al., 2010), has been controversial in the past (Long, 2016, and references therein). However, in both cases an E–W oriented flow will be present beneath our study area, either due to a toroidal flow induced by rollback subduction, or a return flow through a slab gap.

10.1029/2021GC010091

3. Method

3.1. Azimuthal Variations for Non-Vertical SKS Incidence

The SWS procedure that explicitly considers non-vertical incidence ($\theta \leq 30°$) has been introduced and tested in Löberich and Bokelmann (2020a) and Löberich and Bokelmann (2020b). This analysis follows a Taylor-series expansion of Davis (2003), based on the Christoffel equation, to model the angular variation of the fast orientation ϕ and delay time Δt expected for SKS and SKKS core-phases. In the following we summarize the main equations, assuming observed anisotropy can be approximated by a horizontally aligned single-layer, containing minerals of orthorhombic crystal symmetry. Regarding ϕ, the approach considers small oscillations $\delta\phi$ in addition to ϕ_0 (determined for vertical incidence), where

$$\phi = \phi_0 + \delta\phi \tag{1}$$

and

$$\delta\phi = d_1 \ \sin(2z)\theta^2. \tag{2}$$

The additional $\delta\phi$ term leads to angular dependencies, in which the azimuth z introduces a 180°-periodicity, while the incidence θ affects amplitudes. The latter are further influenced by d_1. This oscillation parameter

$$d_1 = -f_1/f_4, \tag{3}$$

where

$$\begin{aligned} f_1 &= C_{1212} - C_{2233} - C_{1133} - 2C_{1313} + C_{1122} - C_{2323} + C_{3333} \text{ and} \\ f_4 &= -2C_{1313} + 2C_{2323}, \end{aligned} \tag{4}$$

contains medium-related information obtained from the stiffness tensor C, and determines the polarity of the phase. Adapting the procedure or Δt leads to

$$\Delta t = \Delta t_0 + e_1\theta^2 + \delta\Delta t \tag{5}$$

and

$$\delta\Delta t = e_2 \ \cos(2z)\theta^2. \tag{6}$$

Here

$$e_1 = \frac{D}{2}\sqrt{\frac{\rho}{\bar{c}^3}}(F_1 - S_1), \text{ and } e_2 = \frac{D}{2}\sqrt{\frac{\rho}{\bar{c}^3}}(F_2 - S_2) \tag{7}$$

where ρ and D denote density and path length respectively,

$$\begin{aligned} F_1 &= -\frac{5}{2}C_{1313} - C_{1133} + \frac{1}{2}C_{1111} + \frac{1}{2}C_{3333} + \frac{1}{2}C_{1212}, \\ F_2 &= -\frac{3}{2}C_{1313} - C_{1133} + \frac{1}{2}C_{1111} + \frac{1}{2}C_{3333} - \frac{1}{2}C_{1212}, \\ S_1 &= -\frac{5}{2}C_{2323} - C_{2233} + \frac{1}{2}C_{2222} + \frac{1}{2}C_{3333} + \frac{1}{2}C_{1212}, \\ S_2 &= \frac{3}{2}C_{2323} + C_{2233} - \frac{1}{2}C_{2222} - \frac{1}{2}C_{3333} + \frac{1}{2}C_{1212}, \\ &\text{and } \bar{c} = \sqrt{C_{1313}C_{2323}}. \end{aligned} \tag{8}$$

Based on these equations, a change of the shear-plane of deformation, and thus the orientation of the symmetry axes, can be detected (Löberich & Bokelmann, 2020a). For the case of a horizontal a-axis (e.g., Nicolas & Christensen, 1987), we can distinguish between either a vertically oriented b- or c-axis (assuming single-crystal A-type olivine, with elastic constants based on San Carlos olivine after Abramson et al., 1997), because these two cases lead to opposite d_1 polarity and thus a phase shift in $\delta\phi$. Distinguishing between vertically oriented *b*- versus *c*-axis allowed Löberich and Bokelmann (2020a) to differentiate between an asthenospheric versus a lithospheric origin for anisotropy (Silver, 1996, and references therein). Resolving this difference requires a good backazimuthal coverage of the SWS data set, and (a) a large number of automatically determined measurements (Löberich & Bokelmann, 2020a), or (b) a moderate number of manually determined observations of higher quality (Löberich & Bokelmann, 2020b). Following these experiences, distinguishing between the various olivine fabrics could be possible as well, if we can assume that the anisotropy is due to horizontal simple shear in the asthenospheric upper mantle (an appropriate assumption for our study area).

3.2. Elastic Tensor Calculations

To compute and compare the expected variations of SWS parameters, the stiffness tensors for olivine samples of different fabric types (multi-crystal olivine) under reasonable conditions have to be well known. Here we take advantage of the study by Jung et al. (2006), which considers San Carlos olivine with different hydration levels under deformation pressures between $P = 0.5–2.1$ GPa and temperatures between $T = 1{,}470-1{,}570$ K. Since we aim to constrain the water content in the asthenospheric upper mantle, we focus only on A-, E-, and C-type olivine and do not consider B- or D-type as likely. Jung et al. (2006) subjected samples to simple shear and measured LPO by electron backscattered diffraction (see references therein). To estimate an effective stiffness tensor, the statistical distribution of the orientations of individual grains in the sample has to be combined with a single-crystal stiffness tensor that describes the elasticity of the individual grain. In Jung et al. (2006), stiffness tensors were determined for 5 GPa and 1,573 K, taking advantage of pressure gradients estimated by Abramson et al. (1997). According to Mainprice et al. (2000), we determine (Equation 9) the corresponding density ρ of olivine for $P = 5$ GPa and $T = 1{,}573$ K following Watt (1988), where

$$\rho(P,T) \approx \rho_A \left[(1 + K'/K \cdot dP)^{1/K'}(1 - \bar{\alpha} \cdot dT)\right]. \tag{9}$$

For this approximation, the density $\rho_A = 3{,}449$ kg/m^3 of San Carlos olivine (Abramson et al., 1997) at $P = 3.7$ GPa serves as a reference. We assume a change in pressure of $dP = 1.3$ GPa and an increase in the Bulk modulus from $K(P = 3.7\text{ GPa}) = 146.3–152.8$ GPa at $P = 5.2\,\text{GPa}$ $(K' = dK/dP = 4.33)$. To further consider the effect of enhanced temperatures ($dT = 1{,}273$ K), we include the average thermal expansivity $\bar{\alpha}(T = [300\,\text{K}, 1500\,\text{K}]) \sim 35.5 \cdot 10^{-6}\,\text{K}^{-1}$ after Isaak (1992), based on Suzuki (1975), estimated for $\rho_I = 3{,}353$ kg/m^3. Assuming $\bar{\alpha}(\rho_A) \approx \bar{\alpha}(\rho_I)$ leads to $\rho \sim 3{,}322$ kg/m^3.

Based on the stiffness tensors and the approximated density, Figure 3 represents the related distributions of P-wave velocity V_P (left) and S-wave anisotropy dV_S (including ϕ; right) in hemispheric projection. According to Jung et al. (2006), each type is defined by a different shear plane, (010), (100), and (001) for A- (top), C- (center), and E-type (bottom), in which the dominant slip direction is [100] for A- and E-type and [001] in the case of C-type. Beside the obvious differences among types due to variations in the axes orientations, effects of non-orthorhombic olivine stiffness tensor components became apparent (see Appendix A, Figure A1). These may be due in part to the relatively small shear-strains achieved in the laboratory experiments (~150% strain), which may be insufficient to fully rotate the crystal axes. Furthermore, Jung et al. (2006) suggested that the experimentally produced LPOs may have experienced distortion related to non-ideal deformation geometries, with the actual slip deviating from the applied shear direction. In order to eliminate the non-orthorhombic components from the experimentally derived elastic tensors, we used the decomposition proposed by Browaeys and Chevrot (2004) as implemented in the MATLAB Seismic Anisotropy Toolkit (MSAT) by A. M. Walker and Wookey (2012). We also took advantage of further MSAT functions (Wookey & Walker, 2015c) to adjust the misalignment of the experimentally derived LPOs, such that the symmetry axes in Figure 3 now align with the shear geometry directions X_1, X_2 and X_3, leading to reduced complexity in each of the visualized tensors. The changes in the V_P anisotropy percentages due to

10.1029/2021GC010091

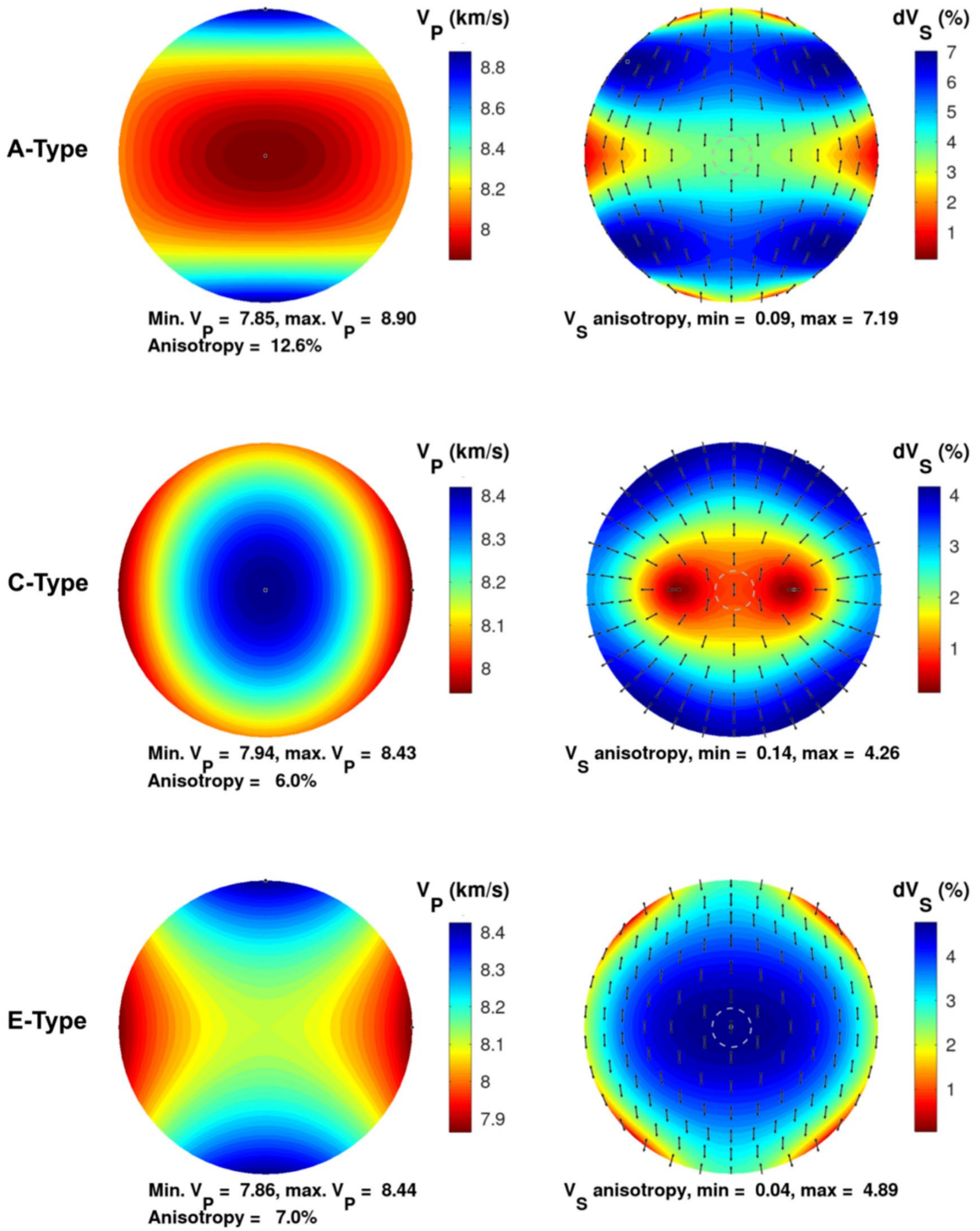

Figure 3. Variation of P-wave velocity V_P and S-wave anisotropy dV_S (including fast orientation ϕ). Gray, dashed circles mark the incidence $\theta \sim 11.88°$, used in Figure 4, for A- (top), C- (center), and E-type (bottom) olivine under upper mantle conditions (5 GPa, 1,573 K). These are based on the decomposed stiffness tensors (without monoclinic and triclinic components) of Jung et al. (2006). X_1 (N–S) and X_2 (E–W) axes define the shear plane in which the shear direction is parallel to X_1. The obtained tensors of orthorhombic symmetry are rotated to X_1, X_2, and X_3.

these adjustments are insignificant (max. 0.4% for A-type). Enhanced V_P values along X_1, for A- and E-type, and X_3, in the case of C-type, are associated with the alignment of olivine's a-axis. Minima along X_2, for C- and E-type, and X_3, considering A-type, indicate the b-axis orientation. In terms of dV_S, the corrections only slightly reduce peak values. Core phases (arrivals inside gray, dashed circles, with nearly vertical propagation directions) experience strongest dV_S anisotropy, expected to elicit most dominant SWS, when traversing

10.1029/2021GC010091

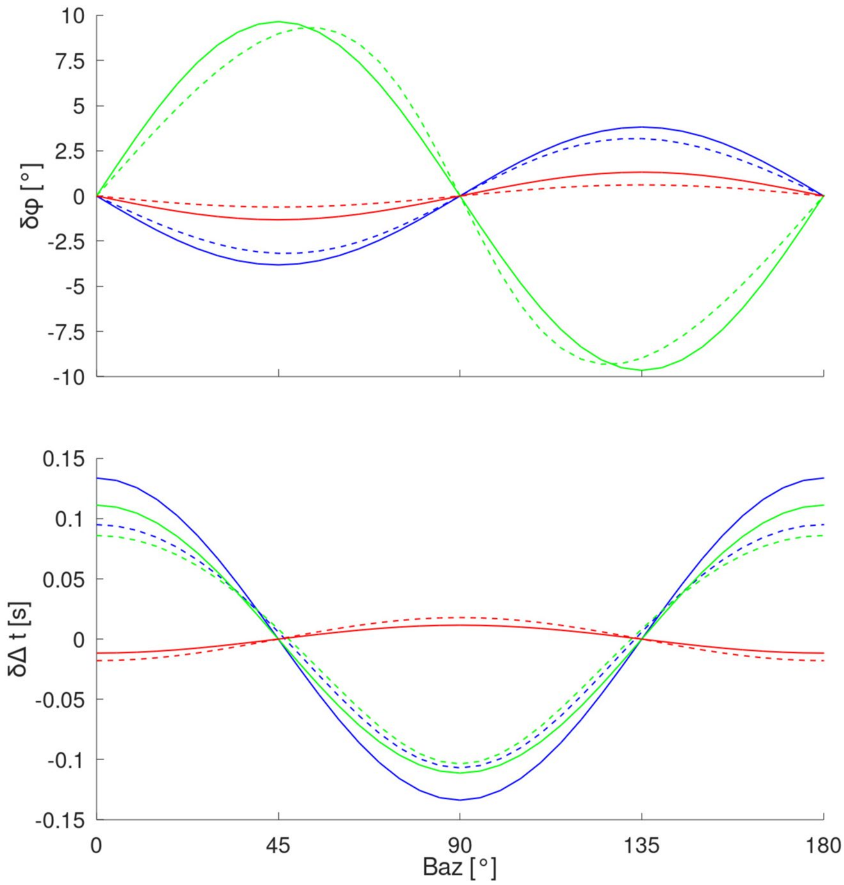

Figure 4. Backazimuthal behavior of shear-wave splitting parameter variations $\delta\phi$ (top) and $\delta\Delta t$ (bottom) based on the Taylor-series expansion (solid lines) of Davis (2003) and the numerical solution (dashed lines) after Mainprice (1990), for a 160 km thick layer (depth: 30–190 km; incidence: $\theta \sim 11.88°$) of A- (blue), C- (green), and E-type (red) olivine (see Figure 3), respectively.

E-type fabric (Karato et al., 2008). As according to Jung et al. (2006), ϕ aligns with the flow direction in all three cases, a similar behavior along X_1 and around X_3 appears for horizontal shearing.

3.3. Backazimuthal Variation of SWS Parameters

To predict the variations of SWS parameters for SKS phases, our model assumes a horizontal layer of either A-, C-, or E-type olivine with a N-S aligned fast orientation. In expectation of increased delay times mentioned before, the presence of a comparably thick layer is expected. As an initial guess, our starting model considers 160 km (30–190 km depth) of anisotropic fabric to be able to match the observed Δt values appropriately. Later in the paper, we will also consider other values for layer thickness (Sections 5.1 and 5.2). Moreover, our comparison between different fabric types requires the assumption of a fixed incidence angle θ. Initially, an incidence angle of ~11.88° (SKS ray parameter 4.919 s/° determined in TauP [Crotwell et al., 1999] using IASP91 [Kennett & Engdahl, 1991]) has been calculated (following Igel, 2006) for the lower boundary. This nominal incidence angle value is approximate, given the actual distance variability of observed SKS/SKKS phases. We emphasize, however, that the actual range of θ for SK(K)S phases is relatively small (10–15° according to Davis, 2003), so this approximation is generally valid (see also Löberich & Bokelmann, 2020a, Appendix E). A smaller incidence angle than that used here would lead to smaller variations in $\delta\phi$ and thus limit the expression of different fabric types in the observations (see Equation 2).

The modeling partly takes advantage of a MSAT example (Wookey & Walker, 2015a), enabling a direct comparison (Figure 4) of our findings (Taylor-series expansion) with the numerically determined variations after Mainprice (1990). Both approaches reveal similar tendencies for the respective stiffness tensor setting, but indicate differences between SWS variations per olivine type. In terms of $\delta\phi$, the C-type variation is shifted against A- and E-type and shows the strongest amplitude. This behavior relates to the differences in polarity and magnitude of the oscillation parameter ($d_{1A} \sim -1.55$; $d_{1C} \sim 3.92$; $d_{1E} \sim -0.54$). Consequently, E-type shows the smallest amplitude. Similarly to d_1, $\delta\Delta t$ is affected by e_2, leading to a comparable variation for A- and C-type ($e_{2A} \sim 3.11$; $e_{2C} \sim 2.59$), and a reversed polarity with smaller amplitudes for E-type ($e_{2E} \sim -0.27$). However, the average Δt of the different types varies significantly. As determined after Mainprice (1990), the A- and C-type stiffness tensors result in mean (and maximum) values of ~1.42 s (~1.51 s) and ~0.35 s (~0.43 s), while an E-type setting can explain Δt values up to ~1.73 s (~1.75 s).

4. Data Analysis and Results

4.1. Shear-Wave Splitting Data Set

To assess the backazimuthal behavior of actual observations with regards to the olivine fabrics, we test the predictions of our A-, C-, and E-type models against SWS measurements in the chosen region of the CSZ back-arc. While a number of studies have been published that examine SWS within or close to our study area (e.g., Long et al., 2009; Schutt et al., 1998; K. T. Walker et al., 2004; Xue & Allen, 2006), for this initial analysis we rely on the SWS-DB-MST data set of Liu et al. (2014), which provides a uniformly processed data set throughout the entire study region. The full database (Western and Central US) comprises > 16000 SWS measurements (14,698 SKS/SKKS) at 1,774 broadband stations (IRIS/USGS Global Seismographic Network, US National Seismic Network, USArray Transportable Array, PASSCAL, GEOSCOPE); used previously in Löberich and Bokelmann (2020a) to establish the extended SWS procedure.

Considering the general behavior of SWS in the central/southern Pacific Northwest (Figure 5 top), the spatial distribution of measurements reveals a consistent pattern and only small dependence on backazimuth. This pattern has been analyzed in detail by Long (2016) and references therein. With respect to the upper mantle beneath the CSZ back-arc, the expected dominant E-W shear direction for a horizontal simple shear deformation (regardless of the drivers of the mantle flow field debated in Long, 2016), yields nearly E-W fast orientations and large delay times (Liu et al., 2014; Long et al., 2009; Wagner & Long, 2013). We select a subset of 1,087 SKS/SKKS measurements within our study area (white polygon in Figure 5 top). Following the respective histograms (Figure 5 bottom), fast orientations and delay times reveal unimodal distributions. Indeed, most SWS measurements align in E-W orientation and tend to higher Δt values of ~1.68 s (variation in Δt is larger than the variation in ϕ). As the expectation of relatively simple anisotropy patterns hold beneath our study region, we can investigate the subtle variations in ϕ that potentially could reflect the olivine fabric type (Figure 4).

4.2. Comparison Between Observations and Predictions

Figure 6 shows the application of the non-vertical incidence SWS approach, following Löberich and Bokelmann (2020a). As the expected difference between A-, C-, and E-type will appear most clearly at respective minima and maxima in the $\delta\phi$ distribution (see Figure 4), variations in the fast orientation hold the highest potential to constrain the olivine fabric type. We therefore focus our analysis on the angular behavior of ϕ; related changes in Δt are shown for completeness in Appendix B. In order to apply our approach, a wide backazimuthal distribution of individual SWS measurements is required. However, seismicity is not homogeneously distributed on Earth, and in the SKS/SKKS distance range, SWS is unlikely to be observed for all possible orientations at a single station. Further, SWS does not occur for null orientations (that is, backazimuths parallel or perpendicular to the fast orientation at which no splitting is expected; see top row in Figure 6, magenta lines). To improve the azimuthal coverage and stabilize the procedure, all stations within our study region are considered jointly, allowing us to combine a large number of splitting measurements into a single analysis. This reveals that southwestern to northwestern backazimuths appear more frequently in our study area. However, even the SWS measurements of neighboring stations could vary around different means $\overline{\phi}$ ($\overline{\Delta t}$). In order to still combine measurements in a straightforward way, we reduce this bias and consider $\delta\phi$ (between −90 and 90°) across all stations (second row; $\delta\Delta t$ accordingly in Figure B1). In this context, only stations with ≥ 5 measurements are investigated to ensure a more stably determined mean

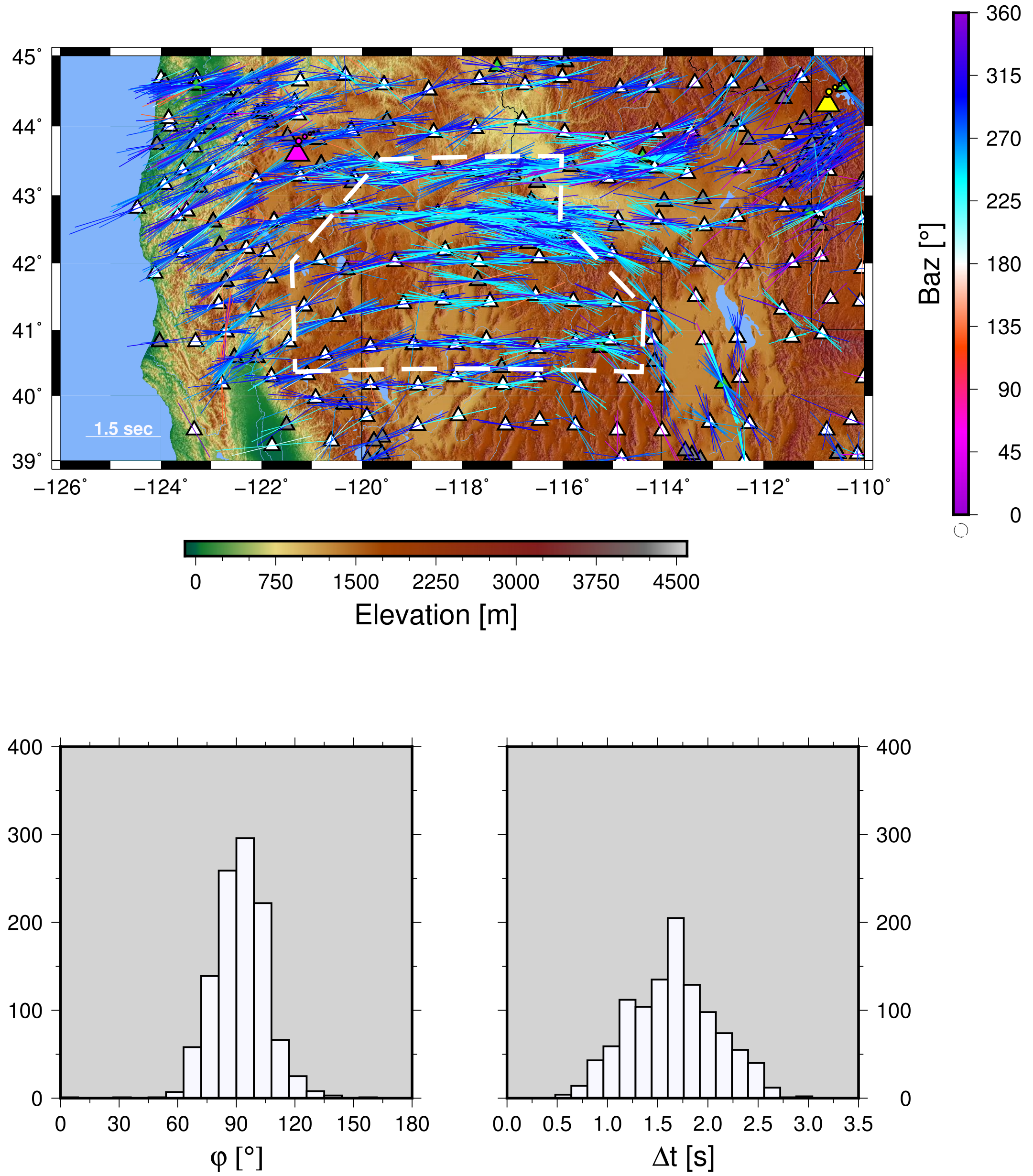

Figure 5. (top) Individual SKS and SKKS shear-wave splitting measurements (lines) at seismic stations (triangles, white: USArray Transportable Array; gray: PASSCAL; green: US National Seismic Network) shown on southern and central Pacific Northwest topography (based on Ferranti & Hormann, 2014). Lines are aligned with the fast orientation ϕ, scaled with delay time Δt and colored by the backazimuth (Baz) of the related earthquake. The study area, Yellowstone and Newberry Caldera are highlighted as in Figure 2. (bottom) Statistical distribution of measured shear-wave splitting parameters ϕ (left) and Δt (right) in the study area indicate unimodal distributions around E-W and ~1.68 s.

value. Since the respective $\overline{\phi}$ per station affects the expected angular variation, the backazimuth of each measurement is corrected for $\bar{\phi}$ as well. This leads to an accumulation of measurements particularly around ~135° and ~225°, which are the dominant intervals in the data set.

Even if the quality of the individual measurements is high (A or B according to Liu et al., 2014), outliers could still bias our investigation. In the following we thus consider only measurements within thresholds, defined by the 0.05 and 0.95 quantile (second row, magenta lines) of both, $\delta\phi$ and $\delta\Delta t$ distribution. Depending on expected minima and maxima positions of $\delta\phi$, our analysis focuses on the more stable variation of

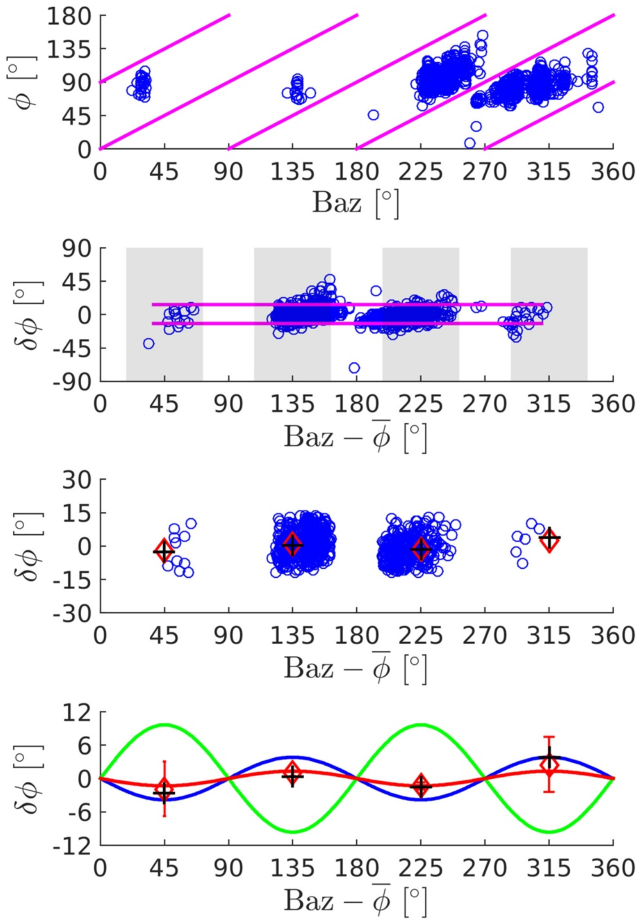

Figure 6. Backazimuthal distribution of fast orientations ϕ in the study area. (top row) Individual shear-wave splitting measurements from all SKS and SKKS phases (solid, magenta lines: Null directions). (second row) Variations $\delta\phi$ from station averages against backazimuths with respect to the average fast orientation per station $\overline{\phi}$. Intervals of interest (±27°) are highlighted (gray shaded); thresholds for $\delta\phi$ (solid, magenta lines) are determined from the distributions. (third row) Means (diamonds) and medians (pluses) of measurements inside thresholds (on $\delta\phi$ and $\delta\Delta t$ see Figure B1) per interval. (bottom row) Derived means (error bars: 2σ-error) and medians compared with expected variations from the Taylor-series expansion (solid lines) in Figure 4 for A-type (blue), C-type (green) and E-type (red) olivine.

mean and median, obtained per interval around 45°, 135°, 225°, and 315°. To avoid biases in the vicinity of null orientations, we limit the interval width. However, the reduced amount of measurements in comparison to Löberich and Bokelmann (2020a) requires less restrictive, wider intervals of ±27° (second row, gray shaded). The resulting means and medians (third row) indicate similar variations for $\delta\phi$, yet means for 135° and 225° are significantly better constrained as in the 45° and 315° intervals due to the enhanced data coverage (bottom row, error bars). Our final comparison between the observed $\delta\phi$ behavior (Figure 6 bottom row) and that predicted by the various models shown in Figure 4 reveals that C-type olivine cannot explain the observed variation, while A- and E-type olivine models are consistent with the data. Even though a differentiation between A- and E-type based on amplitudes is difficult, the better constrained means indicate a tendency to smaller variations, more consistent with the E-type case for our model configuration and assumed incidence angle.

5. Discussion

5.1. Constraints on Olivine Fabric Type and Layer Thickness Beneath Cascadia's Back-Arc

We have demonstrated that even though the effect of non-vertical incidence of SKS and SKKS core phases on splitting parameters is relatively small, it provides an interesting possibility to infer the olivine fabric, assuming a uniform upper mantle. Although this is a crucial restriction, this PNW region might be the "ideal" test region. Considering the lack of backazimuthal variations in apparent splitting parameters (e.g., Wagner & Long, 2013) and the very stable behavior of ϕ with depth from tomographic inversions of splitting measurements (Mondal & Long, 2020), there is good evidence that the anisotropy can be approximated with a single layer, with no depth variability in fast axis orientation. Therefore, we assume that the SWS observations used in our modeling reflect anisotropy in a single layer in the upper mantle, with strain/flow in a nearly E–W direction.

The tendency in $\delta\phi$, particularly in the well constrained 135° and 225° intervals with small 2σ-errors, renders the presence of a 180° periodicity indeed likely. Taking advantage of the expected phase shift in $\delta\phi$ when comparing C-type with A- and E-type enables a differentiation between fabrics and potentially constrains the amount of water in geodynamically active regions (e.g., Karato et al., 2008), subject to some caveats (discussed further below). With respect to the CSZ back-arc, Mondal and Long (2020) have previously argued that hydrated upper mantle conditions should be expected above the slab. However, it remained unclear whether the deformation conditions would facilitate an A-type olivine fabric, for example, proposed by Ohuchi and Irifune (2013), or C-type, following Masuti et al. (2019). Our investigation of the backazimuthal distribution of SWS parameters, based on the large and comprehensive data set of Liu et al. (2014), has shown that C-type olivine cannot explain the observed variations in $\delta\phi$, while A-type, and particularly E-type, can. The analysis of an additional data set from Wagner and Long (2013), a subset of particularly well-constrained stations of the High Lava Plains seismic experiment (see e.g., Long et al., 2009), confirms that a differentiation between A- and E-type on one side, and C-type on the other, is possible in the chosen study area (see Supporting Information S1). Furthermore, our inference on olivine fabric is in agreement with previous indications from the Josephine Peridotite by Skemer et al. (2013). Their investigation of individual Josephine shear zones revealed a change from A- to E-type, accompanied by a change in water content (350–490 ppm H/Si). These findings confirmed previously discovered fabrics by Warren et al. (2008) and Skemer et al. (2010).

Unfortunately, $\delta\Delta t$ does not yield tight constraints that can distinguish between the plausible A-type and E-type fabrics. As E-type predicts the highest Δt values in our model (∼1.75 s for a 160 km thick layer), it seems to be the more likely scenario. However, the trade-off between the thickness and strength of the anisotropic layer prevents specific constraints on both properties. Since the modeled strength of LPOs results from the stiffness tensors estimated by Jung et al. (2006), it is likely representative for upper mantle circumstances; however, changes in the actual amount of strain, which might cause increased strength of anisotropy and larger Δt observations, cannot be ruled out completely. While it is possible that shape-preferred orientation of partial melt in the shallowest upper mantle may affect the measurements too, this effect is likely to be small (Mondal & Long, 2020; Wagner & Long, 2013). We can further assess the likely thickness of the anisotropic layer from tomographic images. For instance, the contours of the relatively strong ≤−3% anomaly in V_S follow a low-velocity body with a maximum thickness of ∼80–90 km beneath our study area. Yet, the low-velocity anomaly could further extend to the Moho (see Long, 2016, and references therein) and anomalies of smaller magnitude in the HLP2010 model might also contribute to the observed delay times. However, due to the reduced resolution of surface waves for depth > 150 km, the bottom of the low-velocity geometry is certainly better constrained by teleseismic body waves. Such studies (e.g., Hawley & Allen, 2019; Schmandt & Lin, 2014; Stanciu & Humphreys, 2020) indeed observed this structure up to ∼200–300 km. Assuming a constant strength of anisotropy, higher Δt values would be directly related to increased layer thickness of the considered dominant single-layer case. Δt measurements around ∼2.48 s (see histogram in Figure 5) could be predicted by a 230 km thick E-type layer (between 30 and 260 km). In this case ($\theta \sim 12.27°$), a mean (and maximum) Δt of ∼2.48 s (∼2.51 s) could be expected, while the same model in A-type configuration leads to ∼2.05 s (∼2.20 s). To obtain similar values for an A-type fabric, a 270 km thick layer (between 30 and 300 km) is required. Such a scenario ($\theta \sim 12.54°$) generates $\Delta t \sim 2.42$ s (∼2.59 s). However, following the model of Karato (2008), A-type is more likely to occur at shallower asthenospheric regions, where lower water contents are expected, while E-type becomes more likely with increasing depth.

5.2. Comparison With Tomography and the Depth Distribution of Anisotropy

If the asthenosphere of the CSZ back-arc is indeed dominated by E-type olivine fabric, then observed fast orientations can be associated with the flow direction, since [100] aligns toward shear direction (Jung et al., 2006; Karato et al., 2008). A comparison of the spatial distribution of SKS splitting measurements at upper mantle piercing points with shear-wave velocity deviations dV/V, for example, resolved by Wagner et al. (2013) based on Rayleigh wave phase observations, provides further insights on the flow geometry (Figure 7 top). The spatial behavior of ϕ in the back-arc correlates with the distribution of a strong low dV/V anomaly, connecting the YSRP with the Northwestern B&R, the HLP, and the CA (see also Figure 2); likely indicating an asthenospheric origin. The dominant clockwise rotation of ϕ toward ESE-WNW in the southern and central part of the study area, which further continues to the southeast, strikingly aligns with the nearly semi-circular shape of the so-called Nevada swirl to the south (Eakin et al., 2010). Toward the northeast, the SWS measurements rather align with the spatial distribution of low-velocities beneath the YSRP. Zhu et al. (2020) have distinguished the decisive flow geometries beneath Pacific Northwest in detail. Their findings agree with a fast slab rollback assumption from Zandt and Humphreys (2008), causing toroidal flow. These flows (below 300 km depths in Zhu et al., 2020) encompass the Gorda slab on one side, while crossing a slab gap further north. In addition, horizontal pressure gradients near the slab gap potentially enable return flows. Beside the flow geometry, the presence of partial melts may affect the dV/V observations. Following Debayle et al. (2020), depths up to 200 km can in principle be affected by decompressional melting (0.3%–0.7%) below back-arc basins or in the vicinity of hotspots. Indeed, Gao and Shen (2014) have interpreted the anomalies beneath Oregon and Nevada as decompressional melts, consistent with the geodynamic model of Long et al. (2012). Regarding Pacific Northwest, Debayle et al. (2020) have further discovered partial melt indications in 300 km depth underneath hotspots. Based on their findings, we determine a depth distribution for our study area (Figure 7 bottom, right). Average melt accumulation reaches a maximum of ∼0.6% at 100 km depth, and another local maximum of ∼0.25% at 300 km depth. Considering the occurrence of melts in greater depth and the flow geometry in the lowermost upper mantle, deeper sources of anisotropy might be possible.

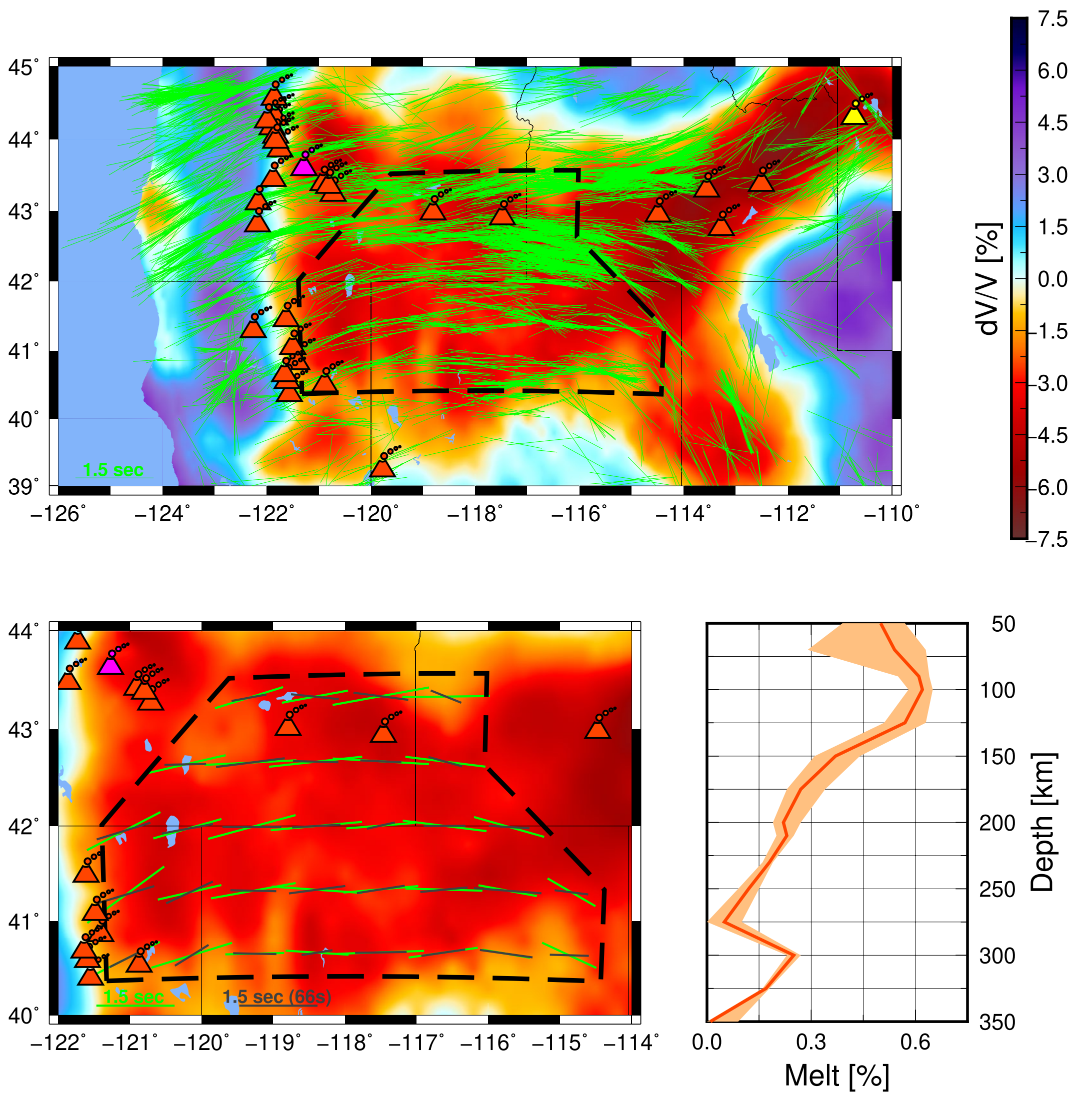

Figure 7. (top) Overlay of individual SKS splitting measurements (green lines) and the distribution of shear-wave velocity variation dV/V at 80 km depth (based on Wagner et al., 2013). Lines are aligned with the orientation of fast wave propagation ϕ, scaled with the delay times Δt and projected to the appropriate piercing points. The dashed, black polygone outlines the study area; volcanos are highlighted as in Figure 2. (bottom, left) Comparison of azimuthal anisotropy (gray lines), determined from phase velocities ($T = 66$ s) by Wagner et al. (2013), with the projected SKS splitting measurements interpolated at reference points. Surface wave anisotropies are aligned with the orientation of fast wave propagation ψ_G and scaled with predicted delay times Δt_{p66s}. (bottom, right) Average melt-depth distribution (orange/red line) including thresholds (orange shade) beneath the study area (based on Debayle et al., 2020).

Since SWS observations integrate the effect of anisotropy along the raypath on the receiver side (e.g., Silver & Chan, 1991), a comparison with a single depth-slice of a tomographic model in the upper mantle can only outline possible relationships. Yet, the distribution of azimuthal anisotropy with depth from surface waves can further elucidate the lateral variation or consistence of the flow field, helping to provide context for our inferences. Figure 7 (bottom, left) shows the comparison between spatially interpolated SKS splitting measurements (from 80 km piercing points) and fast orientations ψ_G from surface waves ($T = 66$ s) at related reference points in the model of Wagner et al. (2013). Generally, the obtained SWS pattern remains oriented E–W near the center of the region and keeps the clockwise rotation at the edges of the study area. The correlation between both indicators supports the assumption of consistent azimuthal anisotropy due to a single-layer case. However, the predicted delay times Δt_{p66s} (calculated in Text S2 of Supporting Information S1 based on Montagner & Nataf, 1986; Montagner et al., 2000; Silver & Chan, 1988; M. L. Smith

& Dahlen, 1973; Vinnik et al., 1989; Weeraratne et al., 2007) for the initially assumed 160 km thick layer tend to be smaller (~0.55–1.33 s) than the interpolated SWS Δt (~0.93–1.88 s). The magnitude of azimuthal anisotropy as constrained by surface waves cannot explain the large Δt; this dilemma was also discussed by Wagner and Long (2013). A recent application of finite-frequency SKS splitting intensity tomography by Mondal and Long (2020) proposed a potential solution to the problem. Their model of the CSZ back-arc includes strong anisotropy (up to ~6%–8%) in the deep upper mantle (200–400 km depth). Surface waves at the period ranges used by Wagner and Long (2013) would not resolve these depths sufficiently, as the sensitivity distribution of the larger periods required would be too broad. A significant contribution to splitting delay times from the deep upper mantle, as suggested by Mondal and Long (2020), on top of the one from a relatively thick layer of E-type olivine fabric in the shallower upper mantle (30–190 km), could explain why the spatial variation of interpolated Δt and amplitudes of vertically integrated travel times *tt* between 30 and 190 km (see Text S2 in Supporting Information S1) do not show a consistent correlation. Beside upper mantle anisotropy, deeper regions might further contribute to observed Δt values (e.g., Savage, 1999). Indications for transition zone anisotropy (>400 km) beneath our area of interest, for example, were revealed just recently by Zhu et al. (2020) and Zhang et al. (2021).

5.3. Water Content of the Asthenosphere

Our finding that the asthenospheric upper mantle beneath the CSZ back-arc is likely dominated by E-type olivine fabric has some important implications. As discussed before, constraints from laboratory experiments suggest the presence of E-type fabric indicates moderately hydrated conditions. Specifically, depending on stress, water contents of ~100–400 ppm H/Si (~360 MPa), ~175–750 ppm H/Si (~190 MPa), ~250–1,100 ppm H/Si (~20 MPa) are expected following Karato et al. (2008), based on Katayama et al. (2004), for temperatures 1,470–1,570 K. We caution, however, that there is some uncertainty as to whether the relationships between deformation conditions and olivine fabric type suggested by laboratory experiments hold for the real Earth. For example, Bernard et al. (2019) studied a suite of xenoliths derived from the mantle lithosphere and found that the olivine fabric type did not correlate with measured water contents in a straightforward way. However, the samples studied by Bernard et al. (2019) were derived from (likely heterogeneous) lithospheric mantle, not the (presumably simpler) asthenospheric upper mantle, and there is some uncertainty as to whether original water contents were preserved in the samples. In any case, however, there are some caveats as to whether olivine fabric type can be interpreted as a straightforward reflection of asthenospheric water content.

If we do take our inference of E-type olivine fabric and a moderately hydrated asthenosphere at face value, then an important question arises: what is the source for the water in the CSZ back-arc? While cold slabs are often assumed to supply water to the deeper mantle (e.g., van Keken et al., 2011), this does not seem to be the controlling factor in the CSZ back-arc given the general reduction of slab seismicity (Canales et al., 2017; Obrebski et al., 2010). Although oceanic crust and mantle lithosphere certainly brought water into the subduction system, the young G-JdF slab (6–8 Myr), characterized by comparatively high temperatures; is assumed to be rather dry (Canales et al., 2017; Currie et al., 2004; Long, 2016; Obrebski et al., 2010; Severinghaus & Atwater, 1990; van Keken et al., 2011), yet petrological findings by Walowski et al. (2015) leave room for discussion on the actual degree of dehydration. Canales et al. (2017) assumes a lower than usually expected amount of water regarding both the lower crust and also mantle portion of the subducting slab. Moreover, upper crustal fluids are already reduced by half at 25 km depth. This behavior generally agrees with the study by van Keken et al. (2011), which expected a rapid dehydration too. The latter investigation assumed that mantle serpentinization will be the last supplier of water at 115 km depth. Even if the slab supplies some modest amount of water beneath the CSZ, it might not directly influence the upper mantle below our study area, given that the slab at this position is located within the transition zone (Figure 2). We propose that material influx from the subslab mantle (Figure 8), which is likely dominated by subslab entrainment (Eakin et al., 2019) and anticipated to be relatively hydrated, toward the mantle above the slab in the back-arc might explain the moderately high water contents. A combination of poloidal and toroidal flow in the CSZ system, suggested by several authors (e.g., Long, 2016; Zandt & Humphreys, 2008; Zhou et al., 2018; Zhu et al., 2020), may play a role in transporting and distributing subslab mantle into the back-arc.

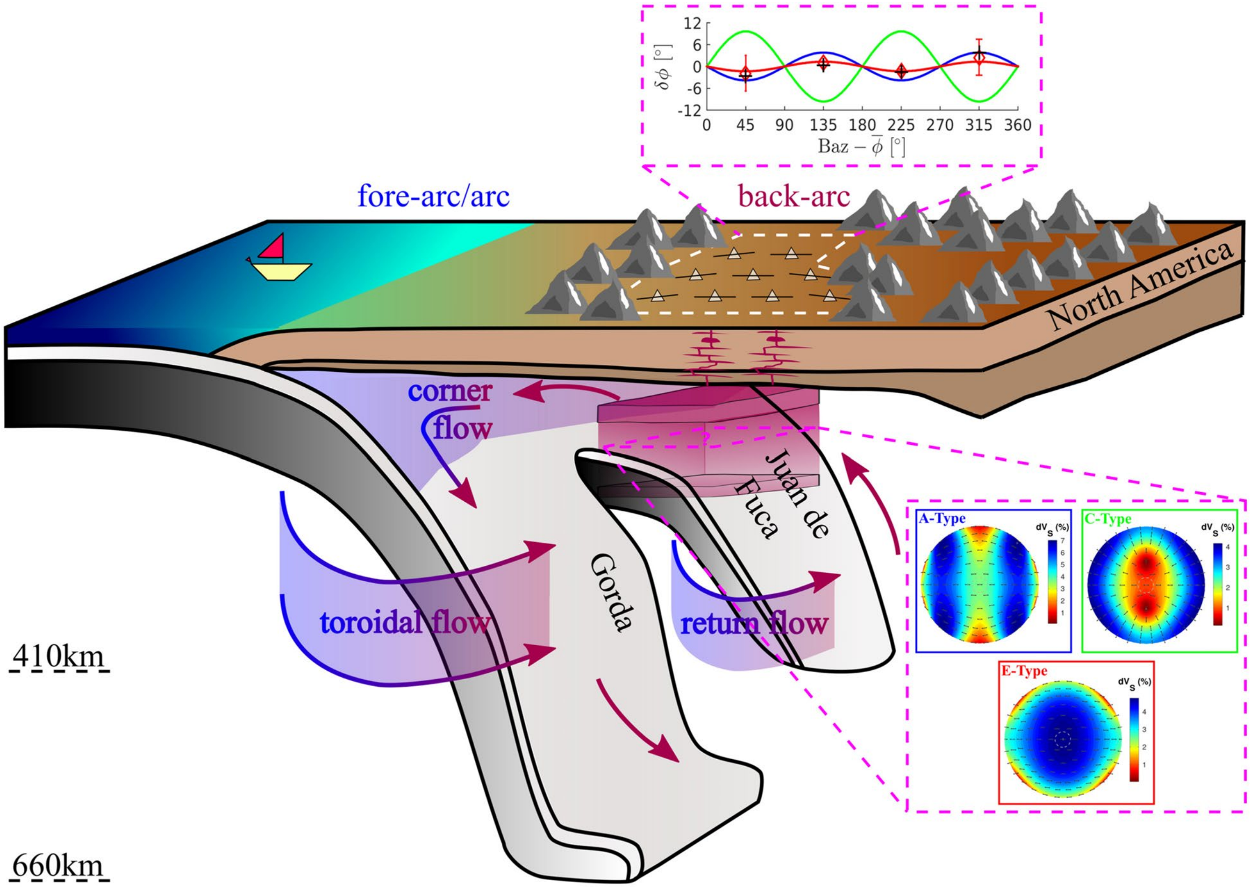

Figure 8. Schematic overview on the interaction between slab geometry and flow system in the Cascadia subduction zone (based on Long et al., 2012; Obrebski et al., 2010; Zhu et al., 2020), and the expected olivine fabric type in the back-arc. A toroidal flow, encompassing the Gorda slab, and a return flow through a possible slab gap transport subslab ambient asthenosphere from the fore-arc/arc to the back-arc. Due to upwelling and the E-W flow system, the oceanic mantle material is distributed beneath the study area (white polygon), and defines the occurring olivine fabric in the low-velocity region (highlighted burgundy). Yet, the presence of either A-, C-, or E-type (right box; hemispheres from Figure 3 rotated in flow direction) could explain the overall observed E-W fast orientation ϕ equally good. However, the comparison between the expected and observed (mean/median) backazimuthal variation in $\delta\phi$ (top box; see Figure 6) shows that E-type, and thus a moderately hydrated asthenosphere, is most probable.

The water content and dominant olivine fabric that would actually be expected in the ambient oceanic asthenosphere is controversial. Based on previous petrological findings from mid-ocean ridge basalts, Jung et al. (2006) concluded their source areas might comprise ∼500–1,000 ppm H/Si; more precise Hirth and Kohlstedt (1996) suggested values of 810 ± 490 ppm H/Si. Following the inference in Jung et al. (2006), C- or E-type would be expected based on these values. Recently, Eakin et al. (2019) suggested that A- or E-type fabric likely dominates in the region directly beneath Cascadia's slab, where subslab mantle is being entrained. If the subslab mantle is indeed relatively water-rich and transported to the back-arc by the ambient mantle flow field, E-type fabrics beneath our study area are a likely consequence. If this scenario is correct, then the degree of dehydration of asthenosphere due to melting (Karato et al., 2008) in Cascadia's back-arc (Debayle et al., 2020; Gao & Shen, 2014; Long et al., 2012) seems to be relatively small and/or restricted to the shallowest parts of the upper mantle. Hence, we infer that melting has not been extensive enough to reduce the water content of the bulk of the asthenospheric upper mantle sufficiently to favor A-type, rather than E-type, fabric.

5.4. Outlook on Future Regions of Application

We can put our findings on olivine fabric beneath the CSZ back-arc into an overall context based on previous indications from other subduction zones, following petrographic examinations of mantle-derived rocks, SWS measurements and modeling expectations. According to laboratory findings, arguments have been made in the past that olivine fabric transitions between different portions of subduction systems should be expected. Jung et al. (2006) predicted that B-, C-, and E-type occur in convergent margin settings, depending on the respective temperature and hydration conditions (see also Karato, 2004; Kneller et al., 2005). There is some potential for our approach to be applied systematically in different regions of a subduction system (fore-arc, arc, and back-arc) in order to directly detect these transitions in the future. The advent of new data sets from dense broadband arrays, such as the USArray Transportable Array in Alaska and AlpArray in the Alps, will help to facilitate these efforts. However, this may require explicit consideration of dipping structures, which can be achieved by extending the Taylor-series expansion according to Davis (2003).

Since our method allows us to detect olivine fabric types in situ in the upper mantle, it can provide crucial complementary constraints in other subduction zone settings. In particular, a fruitful area for future work is the investigation of detailed SWS patterns in regions such as the Alps and the western Pacific subduction zones where there is previous evidence on olivine fabric transitions from the study of natural peridotite rocks. In the context of Alpine subduction, Jung (2017) compiled such studies, which indeed find evidence for various fabrics. While Frese et al. (2003) discovered C-Type from hydrated samples below Cima di Gagnone, Jung (2009) revealed E-type as well as B-type close to Val Malenco. Considering the Izu-Ogasawara trench, Harigane et al. (2013) revealed indications for the presence of E-type and concluded that slab-induced hydration led to transition of previously occurred A- or D-type fabric. Mehl et al. (2003) documented E-type in rocks from the exhumed Talkeetna arc. Due to expected hydration, and since they observed [100] axes oriented in the flow direction, they argued that E-type is prevalent at asthenospheric depths. Although this fabric type has appeared most frequently in the work of Mehl et al. (2003), D- and A-type were detected too.

The few published studies that attempted to infer olivine fabric types by combining SWS measurements and geodynamic modeling, might also point to interesting new study areas for our method. In this context, Lynner et al. (2017) compared source-side SWS measurements with mantle flow simulations for subduction systems (based on Paczkowski, Montési, et al., 2014; Paczkowski, Thissen, et al., 2014) and inferred that C-type might be dominant in the subslab mantle beneath Central America while for Tonga, E-type explained the measurements significantly better. Terada et al. (2013) linked source-side SWS measurements below South Kyushu to C-type fabric. They further argued that the spatial agreement with detected slow propagation velocities and an increased V_P/V_S ratio (based on Matsubara & Obara, 2011; Matsubara et al., 2008) suggest an acutely hydrated mantle environment.

Our procedure may also be applied to investigate the origin of SWS and the prevalence of different olivine fabric types in various tectonic settings. The inflow of oceanic asthenosphere from the subslab mantle underneath our study area seems to be an important factor in controlling the fabric type beneath the CSZ back-arc. However, fairly little is known about the type actually occurring in the normal oceanic asthenosphere. Future investigations might take advantage of records from Ocean Bottom Seismometer (OBS) deployments to overcome this obstacle. According to Tommasi et al. (1996), anisotropy can be attributed to a single-layer behavior beneath ocean basins if a stationary absolute plate motion can be assumed; in this case, asthenospheric as well as lithospheric fabrics would align and be parallel. Long and Silver (2009) summarized that the suboceanic asthenosphere is most likely A-type fabric, following persuasive anisotropy predictions from different models (based on Becker, 2008; Behn et al., 2004; Conrad et al., 2007). However, Song and Kawakatsu (2013) concluded that the prevalent fabric has a girdle distribution known as AG-type (based on Christensen & Crosson, 1968; Mainprice, 2015; Tommasi et al., 2000). The application of our method in ocean basin environments may help to distinguish among different fabric types in the suboceanic asthenosphere. Promising potential datasets include the Cascadia offshore broadband OBS experiment (Bodmer et al., 2015; Martin-Short et al., 2015), the East Pacific Rise region (Harmon et al., 2004; Wolfe & Solomon, 1998), the NoMelt experiment region beneath the Pacific (Lin et al., 2016), and the Eastern North American Margin broadband OBS experiment (Lynner & Bodmer, 2017; Lynner et al., 2019). Previous work provides first tendencies on dominant olivine fabrics in some of these regions; for example, for the east coast of North America, Lynner and Bodmer (2017) deduced that ϕ maps a margin-parallel mantle flow, assuming an A-, C-, or E-type occurrence offshore (based on Karato et al., 2008). With respect to the lithosphere below the Pacific basin, Russell et al. (2019) argued for A- or E-type olivine fabric following surface wave data and mineral physics-based modeling. Our method may be able to add crucial constraints to reduce the uncertainties in these regions in future studies.

6. Conclusion

We have adapted the non-vertical incidence shear-wave splitting approach of Löberich and Bokelmann (2020a) to constrain the olivine fabric in the upper mantle based on differences in phase and amplitude of the backazimuthal variation of the fast orientation ϕ for A-, C-, and E-type olivine, controlled by the oscillation parameter d_1. This methodology has enabled an investigation of the olivine fabric type in the asthenosphere beneath the southern Cascadia subduction zone back-arc. A comparison between expected and observed $\delta\phi$ variations in our study region has revealed that C-type olivine ($d_{1C} \sim 3.92$) cannot be the dominant origin of azimuthal upper mantle anisotropy beneath our study region. A-type ($d_{1A} \sim -1.55$) and E-type olivine ($d_{1E} \sim -0.53$) both match the observations and represent plausible scenarios. While it is challenging to clearly distinguish between A- and E-type, the agreement with smaller $\delta\phi$ amplitudes and the potential to explain the large delay times observed suggests that E-type is probably the dominant fabric. While a 160 km thick layer (depths between 30–190 km) of E-type fabric can explain delay times Δt of up to ~1.75 s, the larger $\Delta t \sim 2.48$ s would require a 230 km thick layer. This inference is consistent with previous work that suggested a contribution from deep upper mantle anisotropy to SWS observations beneath Cascadia's back-arc, which would clarify why predicted delay times Δt_p from surface wave anisotropy are generally too small to match SWS measurements. Furthermore, it provides a reason why interpolated Δt and vertically integrated travel times tt, determined for an anisotropic layer between 30 and 190 km, do not agree particularly well. The inferred presence of E-type olivine fabric implies a moderately hydrated upper mantle in which the observed ϕ pattern, which is spatially correlated with low-velocity anomalies (possibly affected by the occurrence of partial melts), likely reflects the prevailing mantle flow. We argue that the most likely mechanism to sustain moderate hydration in the Cascadia subduction zone back-arc is through the material inflow of hydrated oceanic subslab mantle, since the subducting Gorda-Juan de Fuca slab itself is relatively young, warm, and likely dry. Following previous findings, this transport is probably accomplished through a combination of toroidal flow around the slab edge and/or flow through a slab window, driven by slab rollback. The inferred moderately hydrated back-arc upper mantle also suggests that the bulk of the asthenospheric volume has not been subjected to partial melting; rather, partial melting may have been confined to relatively small volumes of mantle in its shallowest portion, directly beneath the Moho.

Appendix A: Stiffness Tensor Misalignment

Figure A1 shows hemispheres of the P-wave velocity V_P (left) and the S-wave anisotropy dV_S (including ϕ; right) of the full stiffness tensors of Jung et al. (2006) for A- (top), C- (center), and E-type olivine (bottom). These tensors do not only consist of non-zero orthorhombic elements and their subsets, but also contain monoclinic and triclinic components. Hence, symmetry axes are not perfectly aligned with X_1, X_2, and X_3, which affects the parameter distributions.

To adjust misalignment, we carried out decompositions using MS_decomp by Wookey and Walker (2015b), based on Browaeys and Chevrot (2004), subtracted monoclinic and triclinic elements, and orientated remaining components toward X_1, X_2, and X_3. Resulting alterations are shown subsequently (Figure A2).

10.1029/2021GC010091

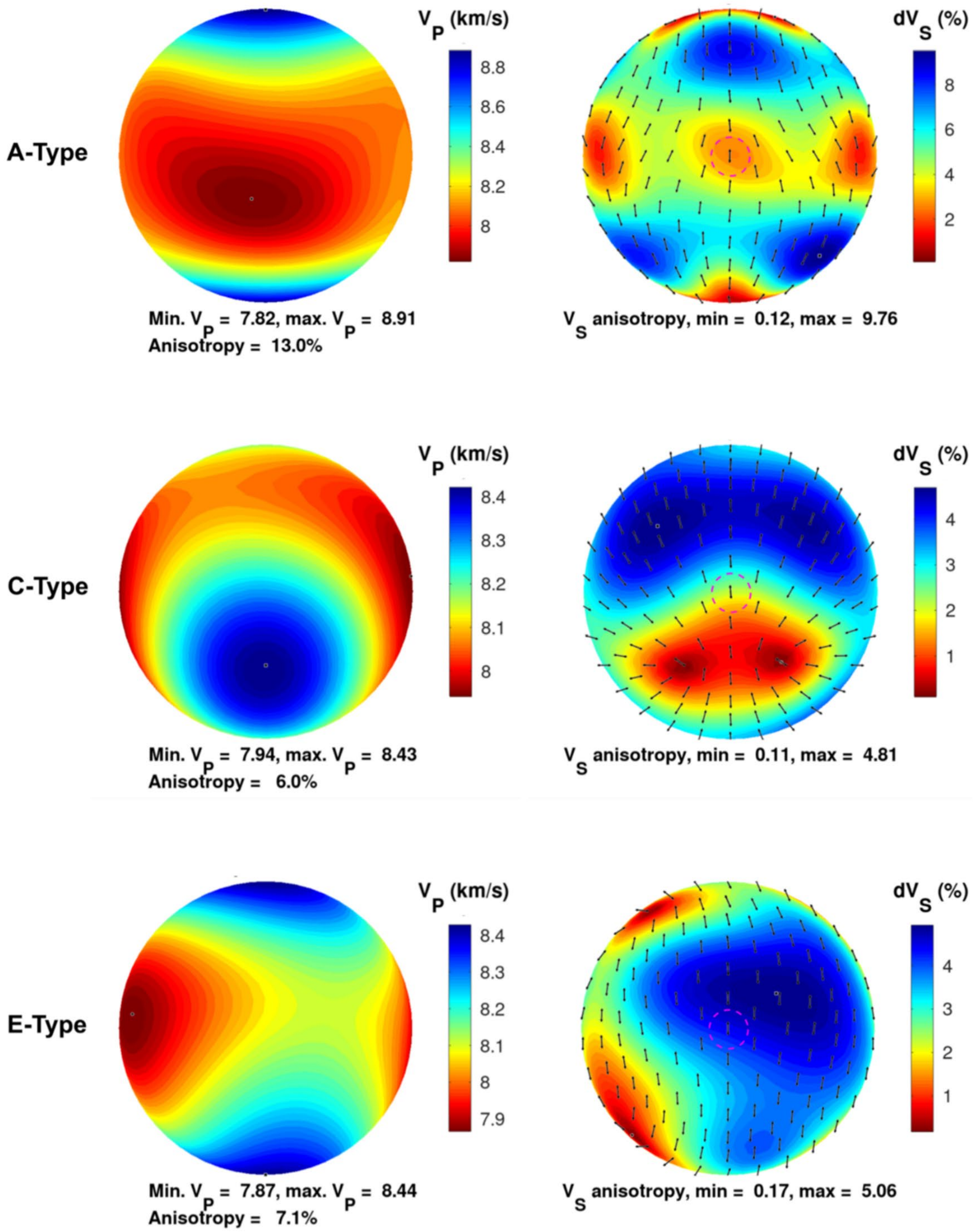

Figure A1. Variation of P-wave velocity V_P and S-wave anisotropy dV_S (including fast orientation ϕ). Magenta, dashed circles mark the incidence $\theta \sim 11.88°$, used in Figure 4, for A-type (top), C-type (center), and E-type olivine (bottom) under upper mantle conditions (5 GPa, 1,573 K). These are based on the full stiffness tensors of Jung et al. (2006). X_1 (N–S) and X_2 (E–W) axes define the shear plane in which the shear direction is parallel to X_1.

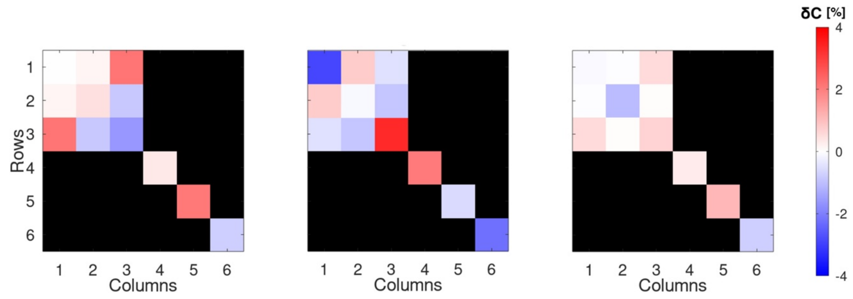

Figure A2. Percentage change from full to orthorhombic olivine stiffness tensor for A-type (left), C-type (center), and E-type (right) of Jung et al. (2006).

Appendix B: Variation of Delay Times Δt With Backazimuth

As indicated in the main text, Figure B1 shows the angular behavior of delay times Δt (top). In accordance with the processing steps for $\delta\phi$, we determine $\delta\Delta t$ along Baz-$\bar{\phi}$ (second row) and introduce thresholds (magenta lines) based on the related distribution (0.05 and 0.95 quantile) to remove outliers. Due to potential biases in the vicinity of Null orientations, more stable means and medians can be determined per interval

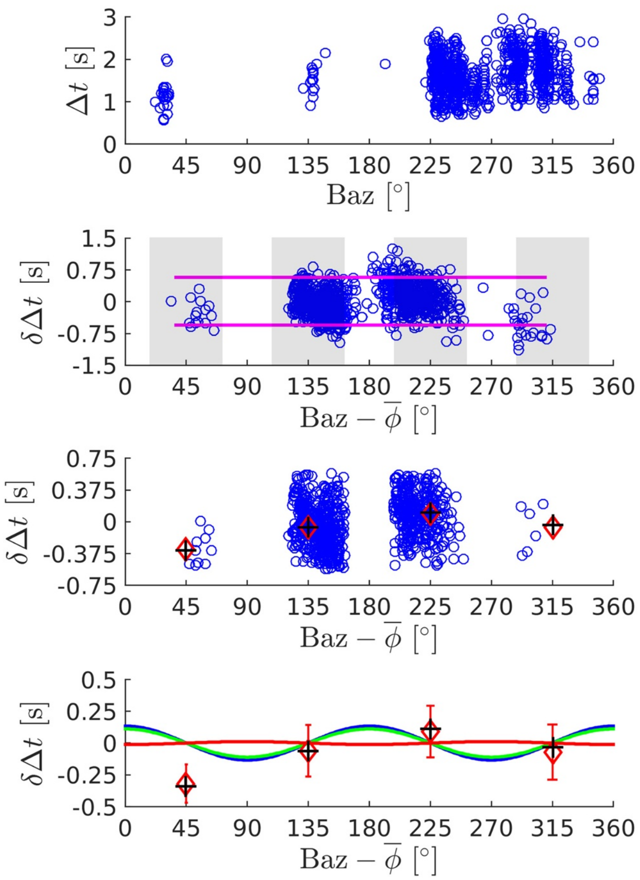

Figure B1. Backazimuthal distribution of delay times Δt in the study area. (top) Individual shear-wave splitting measurements from all SKS and SKKS phases. (second row) Variation $\delta\Delta t$ from station averages in relation to backazimuths with respect to the average fast orientation per station $\bar{\phi}$. Intervals of interest (±27°) are highlighted (gray shaded); thresholds for $\delta\Delta t$ (solid, magenta lines) are determined from the distributions. (third row) Means (diamonds) and medians (pluses) of measurements inside thresholds (on $\delta\Delta t$ and $\delta\phi$ see Figure 6) per interval. (bottom) Derived means (error bars: 2σ-error) and medians compared with expected variations from the Taylor-series expansion (solid lines) in Figure 4 for A-type (blue), C-type (green), and E-type (red) olivine.

(±27°; gray shaded), in which similar variations for $\delta\Delta t$ are indicated (third row). As predicted, $\delta\Delta t$ tends to be ~0 s at the backazimuths of interest (except 45°) and cannot provide further indications on the fabric (bottom). Since the increased amount of measurements around 135° and 225° occurs with a larger variation, the 2σ-errors remain comparable among the different intervals.

Acknowledgments

Our work would not have been possible without the maintenance of several seismographic networks, namely the US National Seismic Network (10.7914/SN/US), the USArray Transportable Array (10.7914/SN/TA), the IRIS/USGS Global Seismographic Network (10.7914/SN/IU), GEOSCOPE (10.18715/GEOSCOPE), and the PASSCAL-supported HLP project (10.7914/SN/XC_2006). The authors further thank Liu et al. (2014) for sharing the related SWS measurements on IRIS DMC (2012). With respect to the presented GMT maps, the authors acknowledge Amante and Eakins (2009) and Ferranti and Hormann (2014) for providing topographies; Bird (2003) and the Smithsonian Institution GVP (2002) for plate boundaries and volcano positions; Debayle et al. (2020) (host: IRIS DMC, 2020) and Hayes et al. (2018) for the melt- and slab-depth distribution. The authors particularly thank Jung et al. (2006) for determining stiffness tensors per olivine type, which have served as the basis of our investigation. The computations in our study have been performed in MATLAB/Octave, taking advantage of MSAT (A. M. Walker & Wookey, 2012) and CircStat (Berens, 2009). SKS incidence angles (following Igel, 2006) and piercing points have been determined using TauP (Crotwell et al., 1999), considering IASP91 (Kennett & Engdahl, 1991) hosted by IRIS (2011). This study has been partly funded by the Austrian Science Fund (FWF) project number P26391 and P30707; E. Löberich received further support through a Dissertation Completion Fellowship by the University of Vienna. The facilities of the IRIS Consortium are supported by the U.S. National Science Foundation (NSF) via grant EAR-1261681. E. Löberich wrote the original draft and is responsible for the work presented here. All co-authors were involved in reviewing and editing tasks. M. D. Long supplied shear-wave splitting measurements of the High Lava Plains project and the related visualization code (see Wagner & Long, 2013). L. S. Wagner provided surface wave tomography models and findings on azimuthal anisotropy (see Wagner et al., 2010; Wagner et al., 2013). E. Qorbani contributed the basic GMT script to visualize shear-wave splitting measurements on topographic maps. G. Bokelmann was involved as supervisor. The views expressed herein are those of the authors and do not necessarily reflect the views of the CTBTO Preparatory Commission.

Data Availability Statement

All data sources and software products, used in this study, are referenced in detail in the Acknowledgments.

References

Abramson, E. H., Brown, J. M., Slutsky, L. J., & Zaug, J. (1997). The elastic constants of San Carlos olivine to 17 GPa. *Journal of Geophysical Resarch: Solid Earth*, *102*(B6), 12253–12263. https://doi.org/10.1029/97JB00682

Amante, C., & Eakins, B. W. (2009). *ETOPO1 1 arc-minute global relief model: Procedures, data sources and analysis. NOAA technical memorandum NESDIS NGDC-24*. National Geophysical Data Center, NOAA. https://doi.org/10.7289/V5C8276M

Babuska, V., & Cara, M. (1991a). Ch. 1 Introduction. In B. L. N. Kennett, R. Madariaga, R. Marschall, & R. Wortel (Eds.), *Seismic anisotropy in the Earth* (1st ed., pp. 1–3). Springer. https://doi.org/10.1007/978-94-011-3600-6_1

Babuska, V., & Cara, M. (1991b). Ch. 3 Elastic anisotropy of rock-forming minerals and polycrystalline rocks. In B. L. N. Kennett, R. Madariaga, R. Marschall, & R. Wortel (Eds.), *Seismic anisotropy in the Earth* (1st ed., pp. 39–70). Springer. https://doi.org/10.1007/978-94-011-3600-6_3

Becker, T. W. (2008). Azimuthal seismic anisotropy constrains net rotation of the lithosphere. *Geophysical Research Letters*, *35*(5), 1–5. https://doi.org/10.1029/2007GL032928

Behn, M. D., Conrad, C. P., & Silver, P. G. (2004). Detection of upper mantle flow associated with the African Superplume. *Earth and Planetary Science Letters*, *224*(3–4), 259–274. https://doi.org/10.1016/j.epsl.2004.05.026

Berens, P. (2009). CircStat: A MATLAB toolbox for circular statistics. *Journal of Statistical Software*, *31*(10), 1–21. https://doi.org/10.18637/jss.v031.i10

Bernard, R. E., Behr, W. M., Becker, T. W., & Young, D. J. (2019). Relationships between olivine CPO and deformation parameters in naturally deformed rocks and implications for mantle seismic anisotropy. *Geochemistry, Geophysics, Geosystems*, *20*(7), 3469–3494. https://doi.org/10.1029/2019GC008289

Bernard, R. E., Schulte-Pelkum, V., & Behr, W. M. (2021). The competing effects of olivine and orthopyroxene CPO on seismic anisotropy. *Tectonophysics*, *814*, 1–10. https://doi.org/10.1016/j.tecto.2021.228954

Bird, P. (2003). An updated digital model of plate boundaries. *Geochemistry, Geophysics, Geosystems*, *4*(3), 1–52. https://doi.org/10.1029/2001GC000252

Bodmer, M., Toomey, D. R., Hooft, E. E., Nábelek, J., & Braunmiller, J. (2015). Seismic anisotropy beneath the Juan de Fuca plate system: Evidence for heterogeneous mantle flow. *Geology*, *43*(12), 1095–1098. https://doi.org/10.1130/G37181.1

Browaeys, J., & Chevrot, S. (2004). Decomposition of the elastic tensor and geophysical applications. *Geophysical Journal International*, *159*(2), 667–678. https://doi.org/10.1111/j.1365-246X.2004.02415.x

Canales, J. P., Carbotte, S. M., Nedimovic, M. R., & Carton, H. (2017). Dry Juan de Fuca slab revealed by quantification of water entering Cascadia subduction zone. *Nature Geoscience*, *10*(11), 864–870. https://doi.org/10.1038/ngeo3050

Christensen, N. I., & Crosson, R. S. (1968). Seismic anisotropy in the upper mantle. *Tectonophysics*, *6*(2), 93–107. https://doi.org/10.1016/0040-1951(68)90013-9

Conrad, C. P., Behn, M. D., & Silver, P. G. (2007). Global mantle flow and the development of seismic anisotropy: Differences between the oceanic and continental upper mantle. *Journal of Geophysical Research: Solid Earth*, *112*(B7), 1–17. https://doi.org/10.1029/2006JB004608

Crotwell, H. P., Owens, T. J., & Ritsema, J. (1999). The TauP Toolkit: Flexible seismic travel-time and ray-path utilities. *Seismological Research Letters*, *70*(2), 154–160. https://doi.org/10.1785/gssrl.70.2.154

Currie, C. A., Cassidy, J. F., Hyndman, R. D., & Bostock, M. G. (2004). Shear wave anisotropy beneath the Cascadia subduction zone and western North America craton. *Geophysical Journal International*, *157*(1), 341–353. https://doi.org/10.1111/j.1365-246X.2004.02175.x

Darold, A., & Humphreys, E. (2013). Upper mantle seismic structure beneath the Pacific Northwest: A plume-triggered delamination origin for the Columbia River flood basalt eruptions. *Earth and Planetary Science Letters*, *365*, 232–242. https://doi.org/10.1016/j.epsl.2013.01.024

Davis, P. M. (2003). Azimuthal variation in seismic anisotropy of the southern California uppermost mantle. *Journal of Geophysical Research: Solid Earth*, *108*(B1), 24-1–24-18. https://doi.org/10.1029/2001JB000637

Debayle, E., Bodin, T., Durand, S., & Ricard, Y. (2020). Seismic evidence for partial melt below tectonic plates. *Nature*, *586*(7830), 555–559. https://doi.org/10.1038/s41586-020-2809-4

Druken, K. A., Long, M. D., & Kincaid, C. (2011). Patterns in seismic anisotropy driven by rollback subduction beneath the High Lava Plains. *Geophysical Research Letters*, *38*(13). https://doi.org/10.1029/2011GL047541

Eakin, C. M., Obrebski, M., Allen, R. M., Boyarko, D. C., Brudzinski, M. R., & Porritt, R. (2010). Seismic anisotropy beneath Cascadia and the Mendocino triple junction: Interaction of the subducting slab with mantle flow. *Earth and Planetary Science Letters*, *297*, 627–632. https://doi.org/10.1016/j.epsl.2010.07.015

Eakin, C. M., Wirth, E. A., Wallace, A., Ulberg, C. W., Creager, K. C., & Abers, G. A. (2019). SKS splitting beneath Mount St. Helens: Constraints on subslab mantle entrainment. *Geochemistry, Geophysics, Geosystems*, *20*(8), 4202–4217. https://doi.org/10.1029/2019GC008433

Ferranti, J. d., & Hormann, C. (2014). *Digital elevation data – World coverage map*. Retrieved from http://www.viewfinderpanoramas.org/Coverage%20map%20viewfinderpanoramas_org3.htm

Ford, M. T., Grunder, A. L., & Duncan, R. A. (2013). Bimodal volcanism of the High Lava Plains and Northwestern Basin and Range of Oregon: Distribution and tectonic implications of age-progressive rhyolites. *Geochemistry, Geophysics, Geosystems*, *14*(8), 2836–2857. https://doi.org/10.1002/ggge.20175

Frese, K., Trommsdorff, V., & Kunze, K. (2003). Olivine [100] normal to foliation: Lattice preferred orientation in prograde garnet peridotite formed at high H_2O activity, Cima di Gagnone (Central Alps). *Contributions to Mineralogy and Petrology*, *145*(1), 75–86. https://doi.org/10.1007/s00410-002-0434-x

Gao, H., & Shen, Y. (2014). Upper mantle structure of the Cascades from full-wave ambient noise tomography: Evidence for 3D mantle upwelling in the back-arc. *Earth and Planetary Science Letters*, *390*, 222–233. https://doi.org/10.1016/J.EPSL.2014.01.012

Gripp, A. E., & Gordon, R. G. (2002). Young tracks of hotspots and current plate velocities. *Geophysical Journal International*, *150*(2), 321–361. https://doi.org/10.1046/j.1365-246X.2002.01627.x

Grunder, A., Johnson, J., Wells, R., & Sanville, H. (2017). *Cenozoic volcanism in the Pacific Northwest (55 my in a complex tectonic setting)*. Retrieved from https://www.iris.edu/hq/inclass/uploads/videos/A-009_PNW_55MY_volcanic_evolution.mp4

Harigane, Y., Michibayashi, K., Morishita, T., Tani, K., Dick, H. J. B., & Ishizuka, O. (2013). The earliest mantle fabrics formed during subduction zone infancy. *Earth and Planetary Science Letters*, *377–378*, 106–113. https://doi.org/10.1016/j.epsl.2013.06.031

Harmon, N., Forsyth, D. W., Fischer, K. M., & Webb, S. C. (2004). Variations in shear-wave splitting in young Pacific seafloor. *Geophysical Research Letters*, *31*(15), 1–4. https://doi.org/10.1029/2004GL020495

Hawley, W. B., & Allen, R. M. (2019). The fragmented death of the Farallon plate. *Geophysical Research Letters*, *46*(13), 7386–7394. https://doi.org/10.1029/2019GL083437

Hayes, G. P., Moore, G. L., Portner, D. E., Hearne, M., Flamme, H., Furtney, M., & Smoczyk, G. M. (2018). Slab2, a comprehensive subduction zone geometry model. *Science*, *362*(6410), 58–61. https://doi.org/10.1126/science.aat4723

Hess, H. H. (1964). Seismic anisotropy of the uppermost mantle under oceans. *Nature*, *203*(4945), 629–631. https://doi.org/10.1038/203629a0

Hirschmann, M. M. (2006). Water, melting, and the deep Earth H_2O cycle. *Annual Review of Earth and Planetary Sciences*, *34*, 629–653. https://doi.org/10.1146/annurev.earth.34.031405.125211

Hirth, G., & Kohlstedt, D. L. (1996). Water in the oceanic upper mantle: Implications for rheology, melt extraction and the evolution of the lithosphere. *Earth and Planetary Science Letters*, *144*(1–2), 93–108. https://doi.org/10.1016/0012-821x(96)00154-9

Igel, H. (2006). *Body waves and ray theory*. Retrieved from https://www.geophysik.uni-muenchen.de/~igel/Lectures/Sedi/sedi_ray.pdf

IRIS. (2011). *iasp91 velocity model (Inactive)*. https://doi.org/10.17611/DP/9991809

IRIS DMC. (2012). *Data Services Products: SWS-DBs Shear-wave splitting databases*. https://doi.org/10.17611/DP/SWS.1

IRIS DMC. (2020). *Data Services Products: EMC-DBRD_NATURE2020*. https://doi.org/10.17611/dp/emc.2020.dbrdnature.1

Isaak, D. G. (1992). High-temperature elasticity of iron-bearing olivines. *Journal of Geophysical Research: Solid Earth*, *97*(B2), 1871–1885. https://doi.org/10.1029/91JB02675

Jung, H. (2009). Deformation fabrics of olivine in Val Malenco peridotite found in Italy and implications for the seismic anisotropy in the upper mantle. *Lithos*, *109*(3–4), 341–349. https://doi.org/10.1016/j.lithos.2008.06.007

Jung, H. (2017). Crystal preferred orientations of olivine, orthopyroxene, serpentine, chlorite, and amphibole, and implications for seismic anisotropy in subduction zones: A review. *Geosciences Journal*, *21*(6), 985–1011. https://doi.org/10.1007/s12303-017-0045-1

Jung, H., & Karato, S.-I. (2001a). Effects of water on dynamically recrystallized grain-size of olivine. *Journal of Structural Geology*, *23*(9), 1337–1344. https://doi.org/10.1016/S0191-8141(01)00005-0

Jung, H., & Karato, S.-I. (2001b). Water-Induced fabric transitions in olivine. *Science*, *293*(5534), 1460–1463. https://doi.org/10.1126/science.1062235

Jung, H., Katayama, I., Jiang, Z., Hiraga, T., & Karato, S.-I. (2006). Effect of water and stress on the lattice-preferred orientation of olivine. *Tectonophysics*, *421*(1–2), 1–22. https://doi.org/10.1016/j.tecto.2006.02.011

Karato, S.-I. (1986). Does partial melting reduce the creep strength of the upper mantle? *Nature*, *319*(6051), 309–310. https://doi.org/10.1038/319309a0

Karato, S.-I. (1987). Ch. 48 Seismic anisotropy due to lattice preferred orientation of minerals: Kinematic or dynamic? In M. H. Manghnani & Y. Syono (Eds.), *High-pressure research in mineral physics: A volume in honor of Syun-iti Akimoto* (1st ed., Vol. 39, pp. 455–471). Wiley. https://doi.org/10.1029/GM039p0455

Karato, S.-I. (1989). Grain growth kinetics in olivine aggregates. *Tectonophysics*, *168*(4), 255–273. https://doi.org/10.1016/0040-1951(89)90221-7

Karato, S.-I. (1995). Effects of water on seismic wave velocities in the upper mantle. *Proceedings of the Japan Academy Series B: Physical and Biological Sciences*, *71*(2), 61–66. https://doi.org/10.2183/pjab.71.61

Karato, S.-I. (2004). Ch. 8 Mapping water content in the upper mantle. In J. Eiler (Ed.), *Inside the subduction factory* (1st ed., Vol. 138, pp. 135–152). Wiley. https://doi.org/10.1029/138GM08

Karato, S.-I. (2008). Ch. 21 Seismic anisotropy and its geodynamic implications. In *Deformation of Earth Materials - An Introduction to the Rheology of Solid Earth* (1st ed., pp. 391–411). Cambridge University Press. https://doi.org/10.1017/CBO9780511804892.022

Karato, S.-I., Jung, H., Katayama, I., & Skemer, P. (2008). Geodynamic significance of seismic anisotropy of the upper mantle: New insights from laboratory studies. *Annual Review of Earth and Planetary Sciences*, *36*, 59–95. https://doi.org/10.1146/annurev.earth.36.031207.124120

Katayama, I., Jung, H., & Karato, S.-I. (2004). New type of olivine fabric from deformation experiments at modest water content and low stress. *Geology*, *32*(12), 1045–1048. https://doi.org/10.1130/G20805.1

Kennett, B. L. N., & Engdahl, E. R. (1991). Traveltimes for global earthquake location and phase identification. *Geophysical Journal International*, *105*(2), 429–465. https://doi.org/10.1111/j.1365-246X.1991.tb06724.x

Kneller, E. A., van Keken, P. E., Karato, S.-i., & Park, J. (2005). B-type olivine fabric in the mantle wedge: Insights from high-resolution non-Newtonian subduction zone models. *Earth and Planetary Science Letters*, *237*(3–4), 781–797. https://doi.org/10.1016/j.epsl.2005.06.049

Lin, P.-Y. P., Gaherty, J. B., Jin, G., Collins, J. A., Lizarralde, D., Evans, R. L., & Hirth, G. (2016). High-resolution seismic constraints on flow dynamics in the oceanic asthenosphere. *Nature*, *535*(7613), 538–541. https://doi.org/10.1038/nature18012

Liu, K. H., Elsheikh, A., Lemnifi, A., Purevsuren, U., Ray, M., Refayee, H., et al. (2014). A uniform database of teleseismic shear wave splitting measurements for the western and central United States. *Geochemistry, Geophysics, Geosystems*, *15*(5), 2075–2085. https://doi.org/10.1002/2014GC005267

Löberich, E., & Bokelmann, G. (2020a). Flow plane orientation in the upper mantle under the Western/Central United States from SKS shear-wave splitting observations. *Geophysical Journal International*, *221*(2), 1125–1137. https://doi.org/10.1093/gji/ggaa060

Löberich, E., & Bokelmann, G. (2020b). Mantle flow under the Central Alps: Constraints from non-vertical SKS shear-wave splitting. *Solid Earth Discussions*, 1–41. https://doi.org/10.5194/se-2020-5

Long, M. D. (2016). The Cascadia Paradox: Mantle flow and slab fragmentation in the Cascadia subduction system. *Journal of Geodynamics*, *102*, 151–170. https://doi.org/10.1016/J.JOG.2016.09.006

Long, M. D., Gao, H., Klaus, A., Wagner, L. S., Fouch, M. J., James, D. E., & Humphreys, E. (2009). Shear wave splitting and the pattern of mantle flow beneath eastern Oregon. *Earth and Planetary Science Letters*, *288*(3–4), 359–369. https://doi.org/10.1016/j.epsl.2009.09.039

Long, M. D., & Silver, P. G. (2009). Mantle flow in subduction systems: The subslab flow field and implications for mantle dynamics. *Journal of Geophysical Research*, *114*(B10). https://doi.org/10.1029/2008JB006200

Long, M. D., Till, C. B., Druken, K. A., Carlson, R. W., Wagner, L. S., Fouch, M. J., et al. (2012). Mantle dynamics beneath the Pacific Northwest and the generation of voluminous back-arc volcanism. *Geochemistry, Geophysics, Geosystems*, *13*(8), 1–22. https://doi.org/10.1029/2012GC004189

Lynner, C., & Bodmer, M. (2017). Mantle flow along the eastern North American margin inferred from shear wave splitting. *Geology*, *45*(10), 867–870. https://doi.org/10.1130/G38980.1

Lynner, C., Long, M. D., Thissen, C. J., Paczkowski, K., & Montési, L. G. J. (2017). Evaluating geodynamic models for sub-slab anisotropy: Effects of olivine fabric type. *Geosphere*, *13*(2), 247–259. https://doi.org/10.1130/GES01395.1

Lynner, C., Van Avendonk, H. J. A., Bécel, A., Christeson, G. L., Dugan, B., Gaherty, J. B., et al. (2019). The eastern North American margin community seismic experiment: An amphibious active- and passive-source dataset. *Seismological Research Letters*, *91*(1), 533–540. https://doi.org/10.1785/0220190142

Mackwell, S. J., Kohlstedt, D. L., & Paterson, M. S. (1985). The role of water in the deformation of olivine single crystals. *Journal of Geophysical Research*, *90*(B13), 11319–11333. https://doi.org/10.1029/jb090ib13p11319

Mainprice, D. (1990). A FORTRAN program to calculate seismic anisotropy from the lattice preferred orientation of minerals. *Computers & Geosciences*, *16*(3), 385–393. https://doi.org/10.1016/0098-3004(90)90072-2

Mainprice, D. (2015). Ch. 2.20 Seismic anisotropy of the deep Earth from a mineral and rock physics perspective. In G. Schubert (Ed.), *Treatise on geophysics* (2nd ed., pp. 487–538). Elsevier. https://doi.org/10.1016/B978-0-444-53802-4.00044-0

Mainprice, D., Barruol, G., & Ismaïl, W. B. (2000). Ch. 11 The Seismic anisotropy of the Earth's mantle: From single crystal to polycrystal. In S.-I. Karato, A. Forte, R. Liebermann, G. Masters, & L. Stixrude (Eds.), *Earth's deep interior: Mineral physics and tomography from the atomic to the global scale* (1st ed., pp. 237–264). Wiley. https://doi.org/10.1029/GM117p0237

Martin-Short, R., Allen, R. M., Bastow, I. D., Totten, E., & Richards, M. A. (2015). Mantle flow geometry from ridge to trench beneath the Gorda-Juan de Fuca plate system. *Nature Geoscience*, *8*(12), 965–968. https://doi.org/10.1038/NGEO2569

Masuti, S., Karato, S.-i., Girard, J., & Barbot, S. D. (2019). Anisotropic high-temperature creep in hydrous olivine single crystals and its geodynamic implications. *Physics of the Earth and Planetary Interiors*, *290*, 1–9. https://doi.org/10.1016/j.pepi.2019.03.002

Matsubara, M., & Obara, K. (2011). The 2011 off the Pacific coast of Tohoku Earthquake related to a strong velocity gradient with the Pacific plate. *Earth, Planets and Space*, *63*(28), 663–667. https://doi.org/10.5047/eps.2011.05.018

Matsubara, M., Obara, K., & Kasahara, K. (2008). Three-dimensional P- and S-wave velocity structures beneath the Japan Islands obtained by high-density seismic stations by seismic tomography. *Tectonophysics*, *454*(1–4), 86–103. https://doi.org/10.1016/j.tecto.2008.04.016

McDonough, W. F., & Rudnick, R. L. (1998). Ch. 4 Mineralogy and composition of the upper mantle. In J. H. Russel (Ed.), *Ultrahigh pressure mineralogy* (1st ed., pp. 139–164). De Gruyter. https://doi.org/10.1515/9781501509179-006

Mehl, L., Hacker, B. R., Hirth, G., & Kelemen, P. B. (2003). Arc-parallel flow within the mantle wedge: Evidence from the accreted Talkeetna arc, south central Alaska. *Journal of Geophysical Research: Solid Earth*, *108*(B8), 4-1–4-18. https://doi.org/10.1029/2002JB002233

Mondal, P., & Long, M. D. (2020). Strong seismic anisotropy in the deep upper mantle beneath the Cascadia backarc: Constraints from probabilistic finite-frequency SKS splitting intensity tomography. *Earth and Planetary Science Letters*, *539*(116172), 1–13. https://doi.org/10.1016/j.epsl.2020.116172

Montagner, J.-P., Griot-Pommera, D.-A., & Lavé, J. (2000). How to relate body wave and surface wave anisotropy? *Journal of Geophysical Research: Solid Earth*, *105*(B8), 19015–19027. https://doi.org/10.1029/2000JB900015

Montagner, J. P., & Nataf, H. C. (1986). A simple method for inverting the azimuthal anisotropy of surface waves. *Journal of Geophysical Research*, *91*(B1), 511–520. https://doi.org/10.1029/JB091iB01p00511

Nicolas, A., & Christensen, N. I. (1987). Ch. 7 Formation of anisotropy in upper mantle peridotites - A review. In K. Fuchs & C. Froidevaux (Eds.), *Composition, structure and dynamics of the lithosphere-asthenosphere system* (1st ed., Vol. 16, pp. 111–123). Wiley. https://doi.org/10.1029/GD016p0111

Obrebski, M., Allen, R. M., Xue, M., & Hung, S.-H. (2010). Slab-plume interaction beneath the Pacific Northwest. *Geophysical Research Letters*, *37*(14), 1–6. https://doi.org/10.1029/2010GL043489

Ohuchi, T., & Irifune, T. (2013). Development of A-type olivine fabric in water-rich deep upper mantle. *Earth and Planetary Science Letters*, *362*, 20–30. https://doi.org/10.1016/j.epsl.2012.11.029

Paczkowski, K., Montési, L. G. J., Long, M. D., & Thissen, C. J. (2014). Three-dimensional flow in the subslab mantle. *Geochemistry, Geophysics, Geosystems*, *15*(10), 3989–4008. https://doi.org/10.1002/2014GC005441

Paczkowski, K., Thissen, C. J., Long, M. D., & Montési, L. G. J. (2014). Deflection of mantle flow beneath subducting slabs and the origin of subslab anisotropy. *Geophysical Research Letters*, *41*(19), 6734–6742. https://doi.org/10.1002/2014GL060914

Qorbani, E., Bianchi, I., & Bokelmann, G. (2015). Slab detachment under the Eastern Alps seen by seismic anisotropy. *Earth and Planetary Science Letters*, *409*, 96–108. https://doi.org/10.1016/j.epsl.2014.10.049

Russell, J. B., Gaherty, J. B., Lin, P. Y. P., Lizarralde, D., Collins, J. A., Hirth, G., & Evans, R. L. (2019). High-resolution constraints on Pacific upper mantle petrofabric inferred from surface-wave anisotropy. *Journal of Geophysical Research: Solid Earth*, *124*(1), 631–657. https://doi.org/10.1029/2018JB016598

Savage, M. K. (1999). Seismic anisotropy and mantle deformation: What have we learned from shear wave splitting? *Reviews of Geophysics*, *37*(1), 65–106. https://doi.org/10.1029/98RG02075

Schellart, W. P., Stegman, D. R., Farrington, R. J., Freeman, J., & Moresi, L. (2010). Cenozoic tectonics of western North America controlled by evolving width of Farallon slab. *Science*, *329*(5989), 316–319. https://doi.org/10.1126/science.1190366

Schmandt, B., & Lin, F.-C. (2014). P and S wave tomography of the mantle beneath the United States. *Geophysical Research Letters*, *41*(18), 6342–6349. https://doi.org/10.1002/2014GL061231

Schutt, D., Humphreys, E. D., & Dueker, K. (1998). Anisotropy of the Yellowstone hot spot wake, eastern Snake River Plain, Idaho. *Pure and Applied Geophysics*, *151*(2–4), 443–462. https://doi.org/10.1007/s000240050122

Severinghaus, J., & Atwater, T. (1990). Ch. 1 Cenozoic geometry and thermal state of the subducting slabs beneath western North America. In B. P. Wernicke (Ed.), *Basin and range extensional tectonics near the latitude of Las Vegas, Nevada* (1st ed., pp. 1–22). Geological Society of America. https://doi.org/10.1130/MEM176-p1

Silver, P. G. (1996). Seismic anisotropy beneath the continents: Probing the depths of geology. *Annual Review of Earth and Planetary Sciences*, *24*(1), 385–432. https://doi.org/10.1146/annurev.earth.24.1.385

Silver, P. G., & Chan, W. W. (1988). Implications for continental structure and evolution from seismic anisotropy. *Nature*, *335*(6185), 34–39. https://doi.org/10.1038/335034a0

Silver, P. G., & Chan, W. W. (1991). Shear wave splitting and subcontinental mantle deformation. *Journal of Geophysical Research: Solid Earth*, *96*(B10), 16429–16454. https://doi.org/10.1029/91JB00899

Skemer, P., Warren, J. M., Hansen, L. N., Hirth, G., & Kelemen, P. B. (2013). The influence of water and LPO on the initiation and evolution of mantle shear zones. *Earth and Planetary Science Letters*, *375*, 222–233. https://doi.org/10.1016/j.epsl.2013.05.034

Skemer, P., Warren, J. M., Kelemen, P. B., & Hirth, G. (2010). Microstructural and rheological evolution of a mantle shear zone. *Journal of Petrology*, *51*(1–2), 43–53. https://doi.org/10.1093/petrology/egp057

Smith, M. L., & Dahlen, F. A. (1973). The azimuthal dependence of Love and Rayleigh wave propagation in a slightly anisotropic medium. *Journal of Geophysical Research*, *78*(17), 3321–3333. https://doi.org/10.1029/jb078i017p03321

Smith, R. B., Jordan, M., Steinberger, B., Puskas, C. M., Farrell, J., Waite, G. P., et al. (2009). Geodynamics of the Yellowstone hotspot and mantle plume: Seismic and GPS imaging, kinematics, and mantle flow. *Journal of Volcanology and Geothermal Research*, *188*(1–3), 26–56. https://doi.org/10.1016/j.jvolgeores.2009.08.020

Smithsonian Institution GVP. (2002). *Global volcano locations database*. Retrieved from https://data.nodc.noaa.gov/cgi-bin/iso?id=gov.noaa.ngdc.mgg.hazards:G02135

Song, T.-R. A., & Kawakatsu, H. (2013). Subduction of oceanic asthenosphere: A critical appraisal in central Alaska. *Earth and Planetary Science Letters*, *367*, 82–94. https://doi.org/10.1016/j.epsl.2013.02.010

Stanciu, A. C., & Humphreys, E. D. (2020). Upper mantle tomography beneath the Pacific Northwest interior. *Earth and Planetary Science Letters*, *539*, 1–14. https://doi.org/10.1016/j.epsl.2020.116214

Suzuki, I. (1975). Thermal expansion of periclase and olivine, and their anharmonic properties. *Journal of Physics of the Earth*, *23*(2), 145–159. https://doi.org/10.4294/jpe1952.23.145

Terada, T., Hiramatsu, Y., & Mizukami, T. (2013). Shear wave anisotropy beneath the volcanic front in South Kyushu area, Japan: Development of C-type olivine CPO under H_2O-rich conditions. *Journal of Geophysical Research: Solid Earth*, *118*(8), 4253–4264. https://doi.org/10.1002/jgrb.50300

Tommasi, A., Mainprice, D., Canova, G., & Chastel, Y. (2000). Viscoplastic self-consistent and equilibrium-based modeling of olivine lattice preferred orientations: Implications for the upper mantle seismic anisotropy. *Journal of Geophysical Research: Solid Earth*, *105*(B4), 7893–7908. https://doi.org/10.1029/1999JB900411

Tommasi, A., Vauchez, A., & Russo, R. (1996). Seismic anisotropy in ocean basins: Resistive drag of the sublithospheric mantle? *Geophysical Research Letters*, *23*(21), 2991–2994. https://doi.org/10.1029/96GL02891

van Houtte, P., & Wagner, F. (1985). Ch. 11 Development of textures by slip and twinning. In H.-R. Wenk (Ed.), *Preferred orientation in deformed metal and rocks: An introduction to modern texture analysis* (1st ed., pp. 233–258). Elsevier. https://doi.org/10.1016/B978-0-12-744020-0.50016-X

van Keken, P. E., Hacker, B. R., Syracuse, E. M., & Abers, G. A. (2011). Subduction factory: 4. Depth-dependent flux of H_2O from subducting slabs worldwide. *Journal of Geophysical Research: Solid Earth*, *116*(B1), 1–15. https://doi.org/10.1029/2010JB007922

Vinnik, L. P., Farra, V., & Romanowicz, B. (1989). Azimuthal anisotropy in the Earth from observations of SKS at GEOSCOPE and NARS broadband stations. *Bulletin of the Seismological Society of America*, *79*(5), 1542–1558.

Wagner, L. S., Forsyth, D. W., Fouch, M. J., & James, D. E. (2010). Detailed three-dimensional shear wave velocity structure of the northwestern United States from Rayleigh wave tomography. *Earth and Planetary Science Letters*, *299*(3–4), 273–284. https://doi.org/10.1016/j.epsl.2010.09.005

Wagner, L. S., Fouch, M. J., James, D. E., & Long, M. D. (2013). The role of hydrous phases in the formation of trench parallel anisotropy: Evidence from Rayleigh waves in Cascadia. *Geophysical Research Letters*, *40*(11), 2642–2646. https://doi.org/10.1002/grl.50525

Wagner, L. S., & Long, M. D. (2013). Distinctive upper mantle anisotropy beneath the High Lava Plains and Eastern Snake River Plain, Pacific Northwest, USA. *Geochemistry, Geophysics, Geosystems*, *14*(10), 4647–4666. https://doi.org/10.1002/ggge.20275

Walker, A. M., & Wookey, J. (2012). MSAT — A new toolkit for the analysis of elastic and seismic anisotropy. *Computers & Geosciences*, *49*, 81–90. https://doi.org/10.1016/j.cageo.2012.05.031

Walker, K. T., Bokelmann, G. H. R., & Klemperer, S. L. (2004). Shear-wave splitting beneath the Snake River Plain suggests a mantle upwelling beneath eastern Nevada, USA. *Earth and Planetary Science Letters*, *222*(2), 529–542. https://doi.org/10.1016/j.epsl.2004.03.024

Walowski, K. J., Wallace, P. J., Hauri, E. H., Wada, I., & Clynne, M. A. (2015). Slab melting beneath the Cascade Arc driven by dehydration of altered oceanic peridotite. *Nature Geoscience*, *8*(5), 404–408. https://doi.org/10.1038/ngeo2417

Warren, J. M., Hirth, G., & Kelemen, P. B. (2008). Evolution of olivine lattice preferred orientation during simple shear in the mantle. *Earth and Planetary Science Letters*, *272*(3–4), 501–512. https://doi.org/10.1016/j.epsl.2008.03.063

Watt, J. P. (1988). Elastic properties of polycrystalline minerals: Comparison of theory and experiment. *Physics and Chemistry of Minerals*, *15*, 579–587. https://doi.org/10.1007/BF00311029

Weeraratne, D. S., Forsyth, D. W., Yang, Y., & Webb, S. C. (2007). Rayleigh wave tomography beneath intraplate volcanic ridges in the South Pacific. *Journal of Geophysical Research: Solid Earth*, *112*(B6), 1–18. https://doi.org/10.1029/2006JB004403

Wenk, H.-R. (Ed.). (1985). *Preferred orientation in deformed metals and rocks: An introduction to modern texture analysis* (1st ed.). Academic Press. https://doi.org/10.1016/C2009-0-21826-5

Wolfe, C. J., & Solomon, S. C. (1998). Shear-wave splitting and implications for mantle flow beneath the MELT region of the East Pacific Rise. *Science*, *280*(5367), 1230–1232. https://doi.org/10.1126/science.280.5367.1230

Wookey, J., & Walker, A. (2015a). *Modelling shear-wave splitting variation with backazimuth*. Retrieved from https://www1.gly.bris.ac.uk/MSAT/doc/examples/splitting_model_example.html

Wookey, J., & Walker, A. (2015b). *MS_decomp - Browaeys and Chevrot decomposition of the elasticity matrix*. Retrieved from https://www1.gly.bris.ac.uk/MSAT/doc/funcs/MS_decomp.html

Wookey, J., & Walker, A. (2015c). *Shear wave splitting*. Retrieved from https://www1.gly.bris.ac.uk/MSAT/doc/MSATfunctions.html

Xue, M., & Allen, R. M. (2006). Origin of the Newberry Hotspot Track: Evidence from shear-wave splitting. *Earth and Planetary Science Letters*, *244*(1–2), 315–322. https://doi.org/10.1016/j.epsl.2006.01.066

Xue, M., & Allen, R. M. (2007). The fate of the Juan de Fuca plate: Implications for a Yellowstone plume head. *Earth and Planetary Science Letters*, *264*(1–2), 266–276. https://doi.org/10.1016/j.epsl.2007.09.047

Yuan, H., & Romanowicz, B. (2010). Depth dependent azimuthal anisotropy in the western US upper mantle. *Earth and Planetary Science Letters*, *300*(3–4), 385–394. https://doi.org/10.1016/j.epsl.2010.10.020

Zandt, G., & Humphreys, E. (2008). Toroidal mantle flow through the western U.S. slab window. *Geology*, *36*(4), 295–298. https://doi.org/10.1130/G24611A.1

Zhang, H., Schmandt, B., & Zhang, J. S. (2021). Localized anisotropy in the mantle transition zone due to flow through slab gaps. *Geophysical Research Letters*, *48*(10), 1–9. https://doi.org/10.1029/2021GL092712

Zhou, Q., Hu, J., Liu, L., Chaparro, T., Stegman, D. R., & Faccenda, M. (2018). Western U.S. seismic anisotropy revealing complex mantle dynamics. *Earth and Planetary Science Letters*, *500*, 156–167. https://doi.org/10.1016/j.epsl.2018.08.015

Zhu, H., Li, X., Yang, J., Stern, R. J., & Lumley, D. E. (2020). Poloidal- and toroidal-mode mantle flows underneath the Cascadia subduction zone. *Geophysical Research Letters*, *47*(14), 1–11. https://doi.org/10.1029/2020GL087530